# Name: Li Gaoyang /李高阳

**Date of Birth**：1990-02-28        **Nationality:** China

**Affiliation:**     Institute of Fluid Science, Tohoku University, Japan

       Graduate School of Biomedical Engineering, Tohoku University, Japan

**Phone:**      +81-07039817029

**E-mail:**      li.gaoyang.e4@tohoku.ac.jp      a798876105@gmail.com

## Education

➤ **2017-2020:** Tohoku University
       Ph. D. student    Biomedical Engineering Major        Advisor: Prof. Makoto Ohta

➤ **2014-2017:** Beijing University of Technology
       M.S. student Biomedical Engineering Major        Advisor: Prof. Qiao Aike

➤ **2010-2014:** Beijing Institute of Technology
       B.S. student Biomedical Engineering Major

## Publications

**Outlines:**

Journal papers: 11     Conference proceedings: 3     Patents: 3

**Journal papers (representative):**

[1] ***Li, G.,*** Song, X., Qiao, A. and Ohta, M., (2018). "Research on arterial stiffness status in type 2 diabetic patients based on pulse waveform characteristics." CMES-Computer Modeling in Engineering and Sciences, 117(2), pp.143-155.

[2] ***Li, G.,*** Watanabe, K., Anzai, H., Song, X., Qiao, A. and Ohta, M., (2019). "Pulse-Wave-Pattern Classification with a Convolutional Neural Network." Scientific reports, 9(1), pp.1-11.

[3] ***Li, G.,*** Wang, H., Zhang, M., Tupin, S., Qiao, A., Liu, Y., Ohta, M., and Anzai, H., (2020.12)"Prediction of 3D cardiovascular hemodynamics before and after coronary artery bypass surgery via deep learning." Nature Communications Biology (accepted).

[4] Wu, D., Wang, S., Xie, J., Mao, B., Li, B., Jin, C., Feng, Y., ***Li, G.***, Liu, Y. (2020) "Hemodynamic Mechanism of Coronary Artery Aneurysm High Occurrence on Right Coronary Artery." Frontiers in Physiology, 11.

[5] Song, X., ***Li, G.,*** Qiao, A., & Chen, Z. (2016). "Association of simultaneously measured four-limb blood pressures with cardiovascular function: a cross-sectional study. " Biomedical engineering online, 15(2), 147.

[6] Song, X., ***Li, G.,*** Qiao, A., Jin, Z., Chen, Z., & You, L. (2019). "Association of Simultaneously Measured Limbs Blood Pressure Differences with Ankle–Brachial Index." International Journal of Computational Methods, 16(03), 1842016.

[7] Li, B., Wang, H., ***Li, G.,*** Liu, J., Zhang, Z., Gu, K., Yang, H., Qiao, A., Du, J. and Liu, Y., (2020). "A patient-specific modelling method of blood circulatory system for the numerical simulation of enhanced external counterpulsation." Journal of Biomechanics, 111, p.110002.

[8] Li, B., Qiao, A., ***Li, G.,*** Ohta, M., & Liu, Y. (2019). "Development of individual algorithm for lumped parameter model of blood circulatory system. " Molecular & Cellular Biomechanics, 16(S2).

[9] Qiao, A., Song, X., Peng, K., Du, G., ***Li, G.,*** & Chen, Z. (2017). "Validity of CAVI measurements for diagnosing hypertension in middle-aged and elderly patients and correlations of these measurements with relevant factors. " Technology and Health Care, 25(S1), 125-134.

[10]Cui, X., Peng, K., Liu, S., Ren, Q., ***Li, G.,*** Gu, Z., & Qiao, A. (2019). "A Computational Modelling of the Mechanical Performance of a Bioabsorbable Stent Undergoing Cyclic Loading. " Procedia Structural Integrity, 15, 67-74.

[11] Cui, X., Ren, Q., Li, Z., Peng, K., **Li, G.,** Gu, Z., & Qiao, A. (2018). "Effect of Plaque Composition on Biomechanical Performance of a Carotid Stent: Computational Study. " Computer Modeling in Engineering & Sciences, 116(3), 455-469

**Conference proceedings:**

[1] ***Li, G.,*** Song, X., Qiao, A. and Ohta, M., "Research on Arterial Stiffness in Type 2 Diabetic Patients Based on Pulse Wave Analysis, " The 15th International Conference on Flow Dynamics. 2018/11/9, Sendai, Miyagi, Japan. (Oral presentation)

[2] ***Li, G.,*** Watanabe, K., Anzai, H., Song, X., Qiao, A. and Ohta, M., "畳み込みニューラルネットワークに基づくアテローム性動脈硬化症患者のパルスパターン認識. " 日本機械学会第 29 回バイオフロンティア講演会，千葉,2018/10/25. (Oral presentation)

[3] ***Li, G.,*** Wang, H., Zhang, M., Ohta, M., and Anzai, H., " Prediction of 3D Cardiovascular Hemodynamics before and after Coronary Artery Bypass Surgery via Deep Learning" The 17th International Conference on Flow Dynamics. 2020/10/29, Sendai, Miyagi, Japan. (Oral presentation)

**Issued patents:**

[1] 安西　晄、渡邉　和浩、***ガオヤン　リー、***太田　信、冨永　悌二、新妻　邦泰、杉山　慎一郎血流場推定装置、学習装置、血流場推定方法及びプログラム.

[2] ***Li, G.,*** Jia, R., Zhang, S., and Qiao, A., "Device with automatic gear regulation function and temperature and bio impedance simultaneous measurement function." 105596001A.

[3] ***Li, G.,*** Song, X., Qiao, A., "Method for calculating heart and vessel functional parameters based on blood pressure and pulses of four limbs." ZL 201610064419.2.

# Academic Experience

➤ **2020-2021(March): Flow Hemodynamics prediction via deep learning**

Research assistant for Prof. Makoto Ohta.

The interventional treatment of cerebral aneurysm requires hemodynamics to provide proper guidance. Computational fluid dynamics (CFD) is gradually used in the calculation of cerebral aneurysm hemodynamics before and after Flow-diverting (FD) stent placement. However, the complex operation (such as the construction and placement simulation of stent) and high computational cost of CFD hinder its application. To solve these problems, we develop aneurysm hemodynamics point cloud data sets and a deep learning network with dual sampling channels. The flexible point cloud format can represent the geometry and flow distribution of different aneurysms with high resolution. The proposed network can directly analyze the relationship between aneurysm geometry and internal hemodynamics, so as to further realize the flow field prediction and avoid the complex operation of CFD. Statistical analysis shows that the prediction results of hemodynamics by our deep learning method are consistent with the CFD method (error function<10%), but the calculation time is reduced by 1800 times. We develop a novel deep learning method, which can accurately predict the hemodynamics of different cerebral aneurysms before and after FD stent placement with low computational cost and simple operation process.

➤ **2018-2020: Flow Hemodynamics prediction via deep learning**

Research assistant for Prof. Makoto Ohta.

The clinical treatment planning of coronary heart disease requires hemodynamic parameters to provide proper guidance. Computational fluid dynamics (CFD) is gradually used in the simulation of cardiovascular hemodynamics. However, for the patient-specific model, the complex operation and high computational cost of CFD hinder its clinical application. To deal with these problems, we develop cardiovascular hemodynamic point datasets and a dual sampling channel deep learning network, which can analyze and reproduce the relationship between the cardiovascular geometry and internal hemodynamics. The statistical analysis shows

that the hemodynamic prediction results of deep learning are in agreement with the conventional CFD method, but the calculation time is reduced 600-fold. In terms of over 2 million nodes, prediction accuracy of around 90%, computational efficiency to predict cardiovascular hemodynamics within 1 second, and universality for evaluating complex arterial system, our deep learning method can meet the needs of most situations.

➢ **2017- 2018: Pulse wave pattern classification via deep learning**

Research assistant for Prof. Makoto Ohta.

Owing to the diversity of pulse-wave morphology, pulse-based diagnosis is difficult, especially pulse-wave-pattern classification (PWPC). A powerful method for PWPC is a convolutional neural network (CNN). It outperforms conventional methods in pattern classification due to extracting informative abstraction and features. For previous PWPC criteria, the relationship between pulse and disease types is not clear. In order to improve the clinical practicability, there is a need for a CNN model to find the one-to-one correspondence between pulse pattern and disease categories. In this part of study, five cardiovascular diseases (CVD) and complications were extracted from medical records as classification criteria to build pulse data set 1. Four physiological parameters closely related to the selected diseases were also extracted as classification criteria to build data set 2. An optimized CNN model with stronger feature extraction capability for pulse signals was proposed, which achieved PWPC with 95% accuracy in data set 1 and 89% accuracy in data set 2. It demonstrated that pulse waves are the result of multiple physiological parameters. There are limitations when using a single physiological parameter to characterise the overall pulse pattern. The proposed CNN model can achieve high accuracy of PWPC while using CVD and complication categories as classification criteria.

➢ **2014-2017: Design and Test of Pulse Wave Measurement Systems**

Research assistant for Prof. Qiao Aike

For patients with type 2 diabetes, the evaluation of pulse waveform characteristics is helpful to understand changes in arterial stiffness. However, there is a lack of comprehensive analysis of pulse waveform parameters. Here, we aimed to investigate the changes in pulse waveform characteristics in patients with type 2 diabetes due to increased arterial stiffness.

In this part of study, 25 patients with type 2 diabetes and 50 healthy subjects were selected based on their clinical history. Age, height, weight, blood pressure, and pulse pressure were collected as the subjects' basic characteristics. The brachial-ankle pulse wave velocity (baPWV) was collected as an index of arterial stiffness. Parameters of time [the pulse wave period (T), the relative positions of peak point (T1) and notch point (T2), and pulse wave time difference between upper and lower limbs (T3)] and area [the total waveform area (A), and the areas of the waveform before (A1) and after (A2) the notch point] were extracted from the pulse wave signals as pulse waveform characteristics. An independent sample t-test was performed to determine whether there were significant differences between groups. Pearson's correlation analysis was performed to determine the correlations between pulse waveform parameters and baPWV.

There were significant differences in T3, A, A1, and A2 between the groups ($P < 0.05$). For patients with type 2 diabetes, there were statistically significant correlations between baPWV and T3, A, A1, and A2 ($P < 0.05$). This study quantitatively assessed changes in arterial pulse waveform parameters in patients with type 2 diabetes. It was demonstrated that pulse waveform characteristics (T3, A, A1, and A2) could be used as

indices of arterial stiffness in patients with type 2 diabetes..

# Representative Publications 1:

# Prediction of 3D Cardiovascular Hemodynamics before and after Coronary Artery Bypass Surgery via Deep Learning

**Gaoyang Li[1,2], Haoran Wang[1,2], Mingzi Zhang[1], Simon Tupin[1], Aike Qiao[3], Youjun Liu[3], Makoto Ohta[1,2,4] Hitomi Anzai[1*]**

[1]Institute of Fluid Science, Tohoku University, 2-1-1, Katahira, Aoba-ku, Sendai, Miyagi ,980-8577, Japan

[2] Graduate School of Biomedical Engineering, Tohoku University 6-6 Aramaki-aza-aoba, Aoba-ku Sendai Miyagi 980-8579, Japan

[3]College of Life Science and Bioengineering, Beijing University of Technology, No.100, Pingleyuan, Chaoyang District, Beijing, 100022, China

[4]ELyTMaX UMI 3757, CNRS–Université de Lyon–Tohoku University

[*]Corresponding author: hitomi.anzai.b5@tohoku.ac.jp

## Abstract

The clinical treatment planning of coronary heart disease requires hemodynamic parameters to provide proper guidance. Computational fluid dynamics (CFD) is gradually used in the simulation of cardiovascular hemodynamics. However, for the patient-specific model, the complex operation and high computational cost of CFD hinder its clinical application. To deal with these problems, we develop cardiovascular hemodynamic point datasets and a dual sampling channel deep learning network, which can analyze and reproduce the relationship between the cardiovascular geometry and internal hemodynamics. The statistical analysis shows that the hemodynamic prediction results of deep learning are in agreement with the conventional CFD method, but the calculation time is reduced 600-fold. In terms of over 2 million nodes, prediction accuracy of around 90%, computational efficiency to predict cardiovascular hemodynamics within 1 second, and universality for evaluating complex arterial system, our deep learning method can meet the needs of most situations.

## Introduction

Coronary heart disease (CHD) has become a leading cause of global mortality[1,2], with more than 50% of these cases being related to coronary stenosis[3]. In order to achieve successful therapeutic effects, CHD clinical treatment plans require a variety of hemodynamic parameters to provide proper guidance. Currently, pressure field-based fractional flow reserve (FFR) is the gold standard for the clinical diagnosis of myocardial ischemia severity caused by stenosis[4-7]. The treatment regimen

guided by FFR has been proven safe and effective[8,9]. For patients with severe myocardial ischemia, revascularization is typically required. Coronary artery bypass grafting (CABG) is the most commonly used revascularization procedure[10]. Velocity field-based postoperative blood flow changes in the grafts and the distal end of the stenotic coronary artery are thought to be the most direct parameter for assessing the influence of CABG[11,12]. However, the application rate of hemodynamic parameters in clinical practice is low, mainly due to its high measurement cost and potential risks during catheter insertion. Taking invasive FFR as an example, the price of the pressure guide wire required for measurement is relatively high. In addition, the use of vasodilator drugs such as adenosine may increase the time and cost of interventional surgery[13], and may also increase the surgical risk of patients with adenosine sensitivity or asthma[14]. Therefore, obtaining hemodynamic parameters including velocity and pressure inexpensively and non-invasively is crucial for the support of CABG and the treatment of CHD.

A large number of previous studies have used computational fluid dynamics (CFD) to obtain cardiovascular hemodynamics[15-19]. Based on the patient's cardiovascular geometry, provided by medical imaging data (e.g., MRI, CT, etc.) and given boundary conditions, CFD can inexpensively and non-invasively obtain solutions for velocity and pressure through the conservation of mass and momentum under isothermal and incompressible assumptions. However, the cost to model cardiovascular hemodynamics with available computational resources is very high[20]. When subjects' personalized CFD boundary conditions (e.g., the inlet is set to pulsatile flow, and the outlet pressure is an invasive measured value) are used to calculate the hemodynamics of complex cardiovascular models with small grafts and coronary branches, even high-performance computational clusters usually require several hours of iteration to ensure the accuracy of the model. Even with simplified boundary conditions (e.g., steady flow at the inlet and zero pressure at the outlet), CFD methods require a calculation time around ten minutes. In addition, each patient's cardiovascular geometry is unique. This means that the CFD procedure will need to be completed separately and repeatedly for each patient. The high computational cost of CFD hinders its clinical application to the treatment of CHD, such as the inability to provide surgical guidance. Therefore, it has become increasingly necessary to develop a cardiovascular hemodynamic calculation method that can reduce calculation costs while ensuring model accuracy.

The development of deep learning, one of many machine learning methods, provides a new way to solve the above problems. Deep learning detects distributed representation features of data by constructing neural networks and combining low-level features to form more abstract high-level

features or attribute features, thus completing the task of classification or regression[21-27]. Advanced deep learning algorithms and high-performance GPU servers can greatly reduce computing times while ensuring high accuracy. Due to the development of deep learning techniques, some studies have introduced its application to predict 2D/3D flow fields from geometrical features. For example, Guo et al. put forward a calculation method of 2D flow around simple geometric models based on convolutional neural networks[28]. And Liang et al. proposed a deep learning method to predict 3D simplified thoracic aortic hemodynamics[29]. However, the research concerning predictions of hemodynamics via deep learning is still very limited[30]. The main limitations of these studies are: 1) most studies focus on 2D flow fields, which have a limited scope of application[31-34], 2) the 3D flow field model only appears in ideal geometry, and sample resolution in the dataset is too low to represent complex flow field distributions and geometric structures[28,29]. For CABG surgery, a cardiovascular model with small grafts and coronary branches has an intricate geometry and internal flow field distribution. Therefore, in this study, in order to accurately predict complex 3D cardiovascular hemodynamics with limited samples, new requirements to adapt to the flexibility and high resolution of the input geometry have been imposed on datasets and deep learning networks, which is also the main technical problem and contribution of this study. Concerning the dataset, each sample must have enough spatial resolution to resolve complex flow field and model geometry. Therefore, it is necessary to find a new, high-resolution sample representation format. And concerning the network, it is necessary to propose a new network structure that can effectively handle the new sample format.

In this study, with the aim of predicting 3D hemodynamics in the real cardiovascular systems of patients with coronary stenosis (e.g., geometry containing aorta, coronary arteries, and bypass graft), we have proposed a new deep learning method which could predict the velocity field and pressure field based on the geometric features of the model. We collected cardiovascular data with small branches from computed tomography angiography (CTA) performed on 110 patients with CHD for model expansion and simulation of CABG surgery. Under certain boundary conditions, a CFD method was used to obtain the hemodynamic results (i.e., velocity and pressure field) of all models. Later, we converted the CFD results into high-density 3D point clouds. The point cloud inherited the ability of CFD results to characterize the geometric structure and flow field distribution of the model, which could characterize the complex flow field distribution and geometry of real cardiovascular models with high resolution[35,36]. On this basis, preoperative and postoperative cardiovascular hemodynamic point datasets were established, respectively. We also proposed a new deep learning

network based on the PointNet structure[37], which could effectively resolve the disorder of point clouds and introduce spatial relationships. By extracting and integrating global and local features of the point cloud, the network could analyze and reproduce the relationship between vessel geometry in the point cloud datasets and the corresponding hemodynamics. The deep learning network only needs to be trained once. Next, when we input cardiovascular geometry information from a new patient, the corresponding 3D hemodynamic parameter prediction results could be obtained within 1 second. In order to verify the accuracy of our deep learning method, we define error functions (ERR), normalized mean absolute error (NMAE), and mean relative error (MRE) to evaluate the difference between the two methods. Based on the acquired hemodynamic results, we further calculated and compared the preoperative FFR and the postoperative blood flow of the graft and the distal stenotic coronary artery. Statistical analysis results showed that the predicted results of deep learning were in agreement with the traditional CFD method, but the calculation time was reduced 600-fold. Our deep learning method aims to realize the prediction of velocity and pressure fields before and after CABG surgery instead of CFD. To the best of our knowledge, this study represents the first report describing deep learning techniques that can effectively and accurately predict 3D hemodynamics of complex cardiovascular system with small grafts and coronary branches with limited data.

## Results

### Prediction results of velocity field

When the preoperative and postoperative velocity field datasets were used as inputs to the proposed deep learning network, the loss function value versus epochs was made available (as seen in Supplementary Fig. 1). The loss function fully converged.

We compared the prediction results of deep learning with CFD. Fig. 1 displays the streamline diagram of a 3D velocity field distribution and a cross-sectional view of velocity magnitude contour in the same areas. It showed that the velocity fields obtained by the two methods had good reliability. Our deep learning method could predict the distribution of velocity fields in the entire cardiovascular model before and after CABG, which included not only general attributes such as laminar blood flow, but also the occurrence of complex vortex structures.
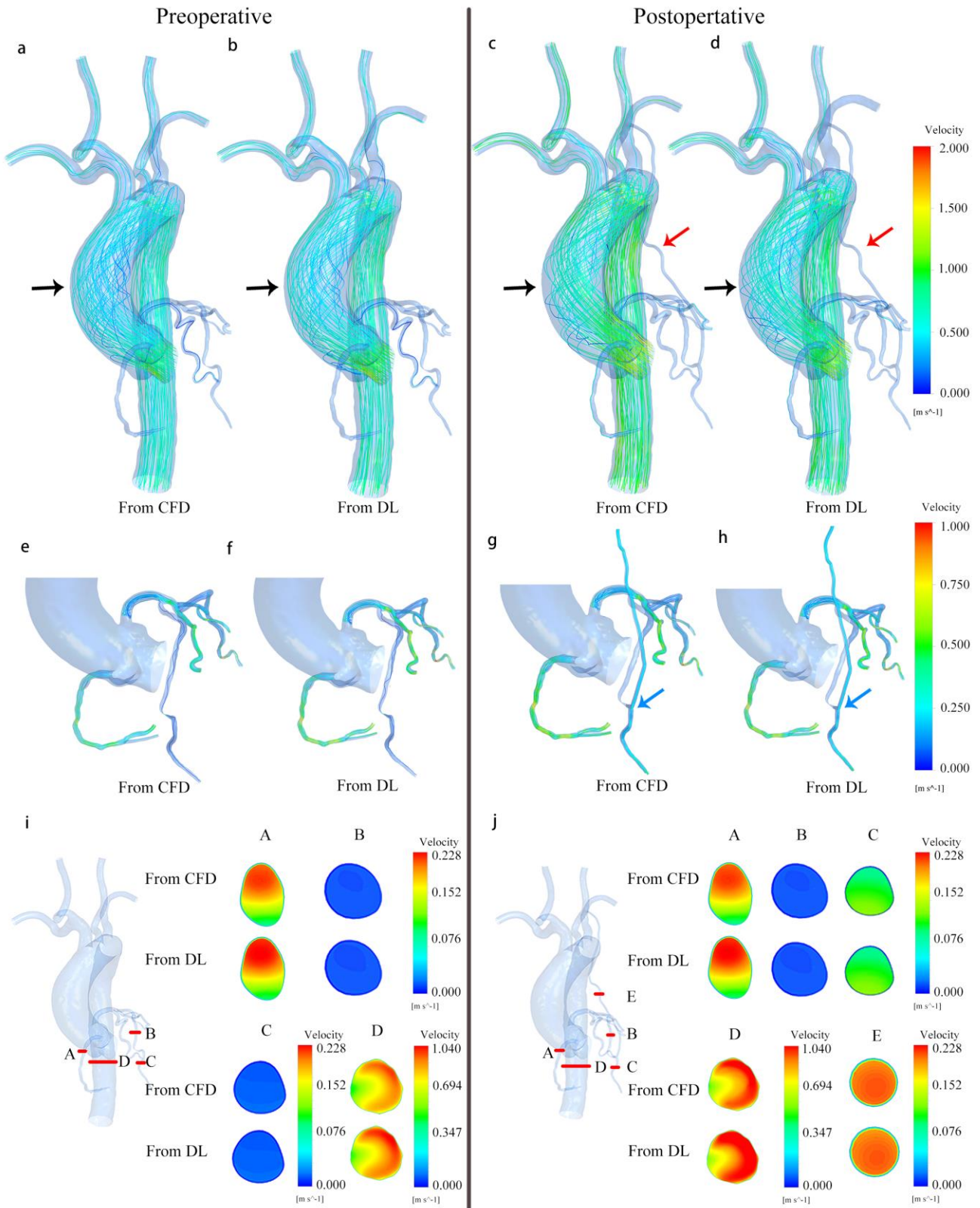
**Fig. 1** Comparison of velocity fields from CFD and deep learning (DL) methods, using a sample with a stenosis rate of 85%. **a-d** are streamline diagrams of the entire cardiovascular internal flow field before and after CABG obtained from CFD and DL. The position indicated by the black arrow in **a-d** is the vortex region of ascending aorta. The position indicated by the red arrow in **c-d** is the grafts. **e-h** are streamline diagrams of the coronary artery and grafts flow field. The blood flow velocity inside the coronary artery is smaller than that in the aorta, which means that it is difficult to

clearly show the distribution of the internal flow field in the coronary artery under the same velocity colour bar. Therefore, the coronary flow field is displayed separately. The position indicated by the blue arrow in **g-h** is the connection site between the graft and the LAD. **i-j** are cross-sectional views of the velocity distribution, respectively from A: RA branch; B: the proximal end of LAD before stenosis; C: the distal end of LAD after stenosis; D: descending aorta; E: graft. E can reflect laminar flow in the graft. The comparison results confirm the high consistency of the velocity field obtained by the two methods. This clearly shows the effect of CABG surgery on the flow field distribution of the entire cardiovascular system.

We calculated the mean value of the predicted velocity field ERR of the 100 models in the test sets, as shown in Table 1. The result showed that the prediction accuracy of the coronary arteries (NMAE ＜3%, MRE＜5%) and grafts (NMAE＜1.5%, MRE＜2.5%) was higher than that of the aorta and superior aortic branch artery (Preoperative: NMAE=6.02%, MRE=9.77%; Postoperative: NMAE=6.01%, MRE=9.74%). This was mainly due to the larger magnitude of flow and the complicated flow field distribution by vortex and flow separation in both the aorta and superior aortic branch artery parts. We give detailed explanations and feasible improvements in the prediction error analysis section below.

Table 1. Performance evaluation of the velocity field

| | ERR(%) | Proximal end of LAD | Distal end of LAD | LCX | RA | Graft | Aorta and superior aortic branch artery |
|---|---|---|---|---|---|---|---|
| Preoperative | NMAE | 2.62±1.47 | 2.53±1.02 | 2.33±1.25 | 2.91±1.64 | | 6.02±2.97 |
| | MRE | 4.12±2.46 | 3.97±2.77 | 4.61±2.13 | 4.35±1.87 | | 9.77±3.86 |
| Postoperative | NMAE | 2.60±1.43 | 2.64±1.25 | 2.33±1.25 | 2.91±1.64 | 1.12±0.57 | 6.01±2.96 |
| | MRE | 4.11±2.42 | 4.21±2.96 | 4.61±2.13 | 4.35±1.87 | 2.01±1.25 | 9.74±3.83 |

Deep learning prediction results (shown in Fig. 1 and Table 1) could reflect the effect of CABG on the distribution of internal flow field in the cardiovascular system. It could accurately reproduce velocity fields in the small lesion coronary and reconstructed grafts, which meant that it could not only reflect the preoperative ischemic condition of LAD branches with different stenosis rates, but also signal the postoperative improvement of blood supply. In addition, it could be seen from the predicted results that CABG had a big impact on the flow field of the grafts and LAD with stenosis but had little influence on the flow field of other parts. The proposed network could effectively

identify significant and non-significant disturbances of the graft on the flow field, which highlighted its high performance.

**Prediction results of pressure field**

This study aimed to develop a universal deep learning method. The same network structure could accomplish predicting hemodynamic parameters with different attributes, which could then be proven via the analysis results of the velocity field and pressure field.

Different from the velocity, the pressure in the flow field was scalar, that was, the pressure at a point had the same value in all directions. There were different vector components of velocity vector in X, Y and Z directions. Therefore, the pressure datasets as the network input contained less information than the velocity field datasets, which was reflected in the convergence speed of the loss function value versus epochs (as seen in Supplementary Fig. 1). The loss function converged faster.

Fig. 2 displays a 3D pressure distribution cloud map obtained from deep learning and CFD method, with a cross-sectional view of the same part. The pressure fields obtained by the two methods were also in agreement. Our deep learning method could accurately replicate the pressure distribution of the entire cardiovascular model with small grafts and coronary branches.
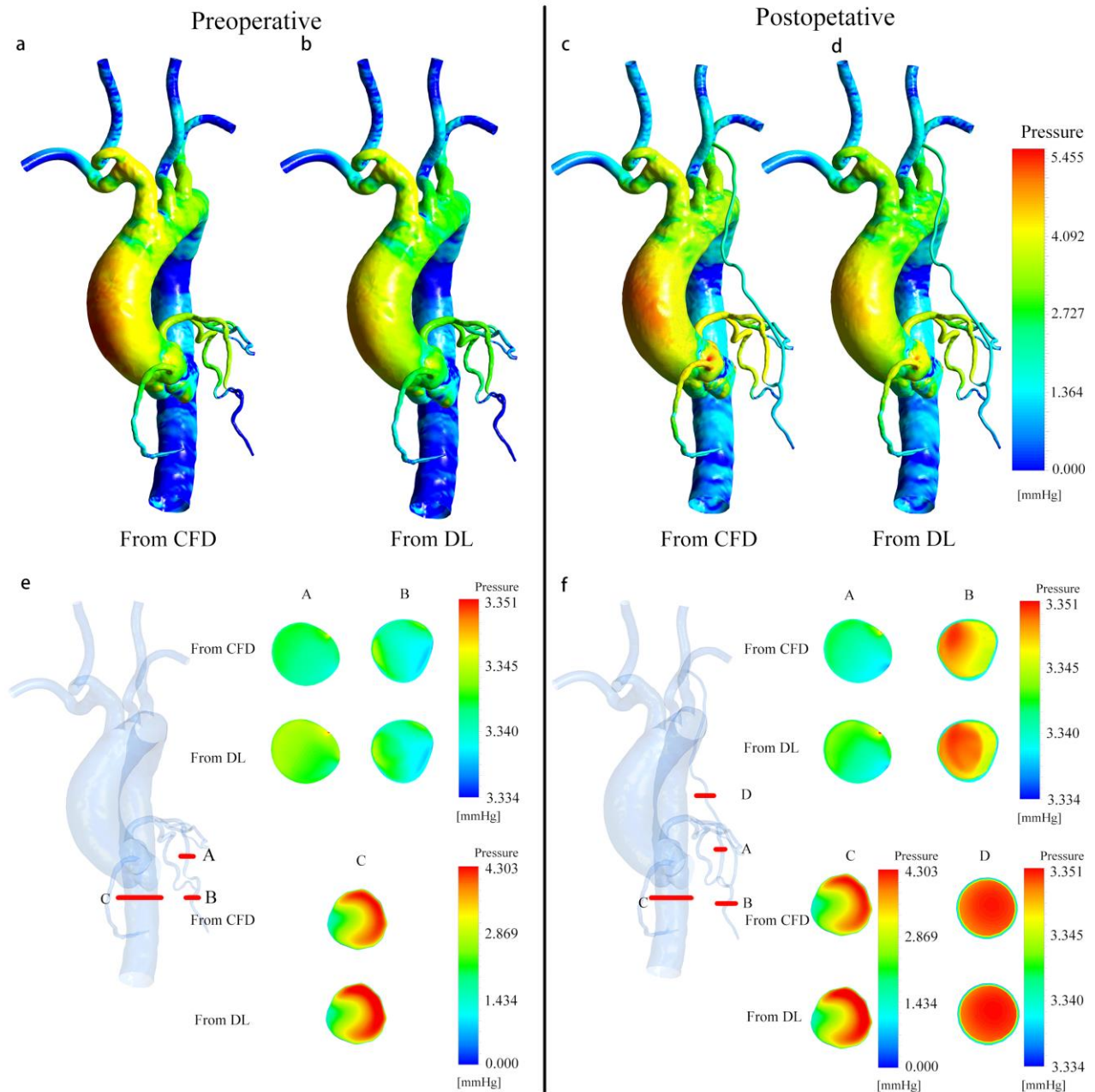
**Fig. 2** Comparison of pressure field from CFD and deep learning (DL), using a sample with a stenosis rate of 85%. Because the CFD outlet boundary was set as zero pressure condition, the pressure value in this figure was actually the pressure difference relative to the coronary outlet. **a-d** are pressure distribution cloud maps of the entire cardiovascular before and after CABG obtained from CFD and DL. **e-f** are cross-sectional views of the pressure distribution, respectively from A: the proximal end of LAD before stenosis; B: the distal end of LAD after stenosis; C: descending aorta; D: graft. The comparison results confirm the high consistency of the pressure field obtained by the two methods. The results of coronary pressure prediction can help us calculate FFR to further evaluate the performance of our deep learning method.

We calculated the mean value of the predicted pressure field ERR of the 100 models in the test set, as shown in Table 2. The prediction accuracy of pressure fields of coronary artery (NMAE＜2.5%, MRE＜4%) and grafts (NMAE＜1.5%, MRE＜2%) was also higher than that of the aorta and superior aortic branch artery (Preoperative: NMAE=4.30%, MRE=7.61%; Postoperative: NMAE=4.28%, MRE=7.35%), as explained in the prediction error analysis section below.

Based on the velocity and pressure field, we calculated important clinical indicators related to CABG surgery: preoperative FFR of the lesion LAD and the postoperative blood flow of the graft and the distal stenotic coronary artery. The performance of our deep learning method could be further evaluated by comparing the indicators obtained by the two methods, which is described in detail below.

Table 2. Performance evaluation of the pressure field

| | ERR(%) | Proximal end of LAD | Distal end of LAD | LCX | RA | Graft | Aorta and superior aortic branch artery |
|---|---|---|---|---|---|---|---|
| Preoperative | NMAE | 2.03±1.13 | 1.83±1.18 | 1.71±1.49 | 2.04±1.12 | | 4.30±1.58 |
| | MRE | 3.55±1.74 | 3.12±1.63 | 3.52±1.97 | 3.63±1.96 | | 7.61±1.99 |
| Postoperative | NMAE | 1.99±1.09 | 1.96±1.31 | 1.71±1.49 | 2.04±1.12 | 1.01±0.47 | 4.28±1.55 |
| | MRE | 3.52±1.72 | 3.57±1.98 | 3.52±1.97 | 3.63±1.96 | 1.98±0.97 | 7.35±1.89 |

**Deep learning improves computing efficiency**

After the training was completed, and when the point coordinate space information of the cardiovascular model in the test set was input to the network, the hemodynamics of the query point could be obtained within 1 second using a NVidia GeForce GTX 1080 Ti GPU. For the CFD method, the calculation time of one model on an Intel Xeon Gold 6148 2.4Ghz $\times$ 2 CPU server was about 10 minutes. Deep learning improved the computational efficiency of a single model 600-fold. Although it took some time (about 40 hours) to complete network training, this process only needs to be completed once to predict the hemodynamic of all models in the given test set. Compared to the traditional CFD method, where each model requires independent simulation calculations, the computational cost of deep learning is far less than CFD.

Together with the accuracy analysis of the results, the proposed deep learning network could efficiently and accurately predict 3D hemodynamics of complex cardiovascular system with small grafts and coronary branches. This also meant that deep learning has broad application prospects, such as the possibility of application in the early planning or even real-time support of CABG.

**Calculate FFR and improved flow based on prediction results**

In order to further confirm the accuracy and clinical utility of our deep learning method, we calculated the preoperative FFR value and postoperative blood flow value of the grafts and the distal end of the stenosis using the hemodynamic results acquired from CFD and deep learning, respectively. The FFR was defined as the ratio of the mean pressure at a cross section 3 cm downstream of the stenosis to the mean pressure at the LAD coronary entry region[38]. Improved blood flow was defined as graft inlet flow, which was calculated based on the diameter and velocity of the graft inlet section. Fig. 3a and 3b were the scatter plots of FFR and improved flow on each model obtained from the two methods, which showed that the correlation between the FFR and improved flow attained from these methods was excellent (FFR: r=0.9580, P<0.001; Flow: r=0.9734, P<0.001). Also, the Bland-Altman analysis result is as shown in Fig. 3c and 3d: 97 sets of FFR data and 97 sets of improved flow data fall within the 95% confidence interval (FFR: -0.07780-0.09254; Flow: -1.282-0.8568), which confirmed that the clinical indicators calculated by these methods were in agreement.

Our deep learning method reduced the computational time of hemodynamics to 1 second, and its output was a point cloud format which was easy to post-process. On this basis, the calculation time of clinical indicators such as FFR and improvement of blood flow could also be reduced to a few seconds while ensuring high accuracy, which further confirmed the superiority of our deep learning method.
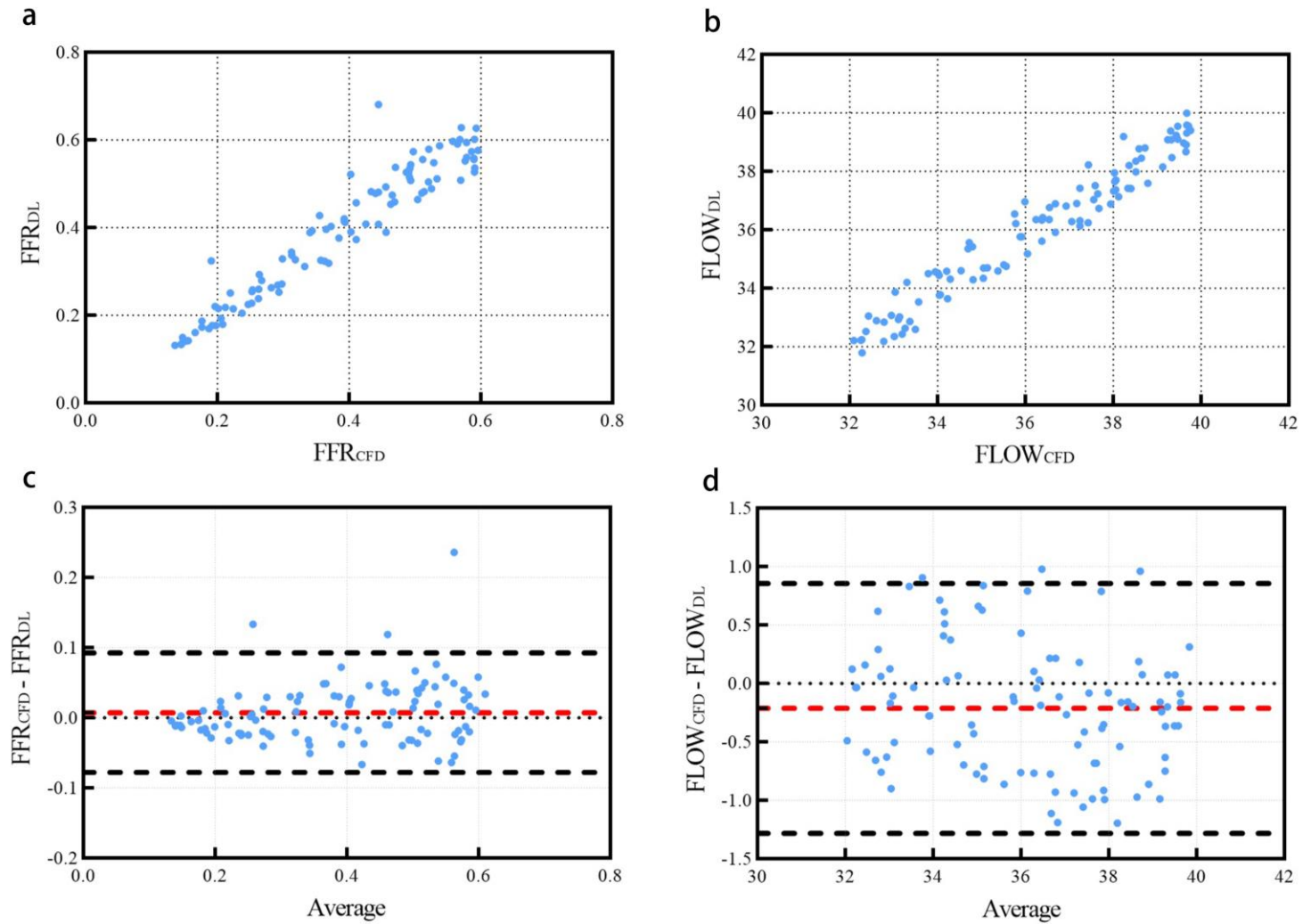
**Fig. 3** Comparison of FFR and improved blood flow obtained from CFD and Deep Learning. **a** is a scatterplot of FFR values from CFD (FFR$_{CFD}$) and deep learning (FFR$_{DL}$). **b** is a scatterplot of improved blood flow values from CFD (FLOW$_{CFD}$) and deep learning (FLOW$_{DL}$). **c-d** are Bland-Altman analysis plot of corresponding **a** and **b**. The hemodynamic results used to calculate FFR and improved blood flow are from 100 cardiovascular models in the test set.

**Prediction error analysis**

We extracted regions with large prediction error function values (MRE>10%) in the entire cardiovascular model. These regions were highly consistent with the vortex regions in the CFD calculation results, as shown in Fig. 4a and 4b. Vortexes were mainly distributed in the aorta and superior aortic branch artery rather than the coronary artery and graft. Points in the aorta and superior aortic branch artery region accounted for more than 99% of the query point cloud, and more than 30% of the points in the whole region were located in the vortex region, which was the main source

of prediction errors for the cardiovascular model. We extracted the points only in the vortex region which was defined with Eigen Helicity method, level 0.005, actual value 44.89 s$^{-1}$ for predicted results and calculated the error as shown in Fig. 4c. The points in the coronary artery and graft part only accounted for 1% of the query point cloud, and only about 10% of them were in the vortex region, which had little effect on the prediction errors. The vortex distribution also explained why the graft and coronary parts had higher prediction accuracy.



a

b

c
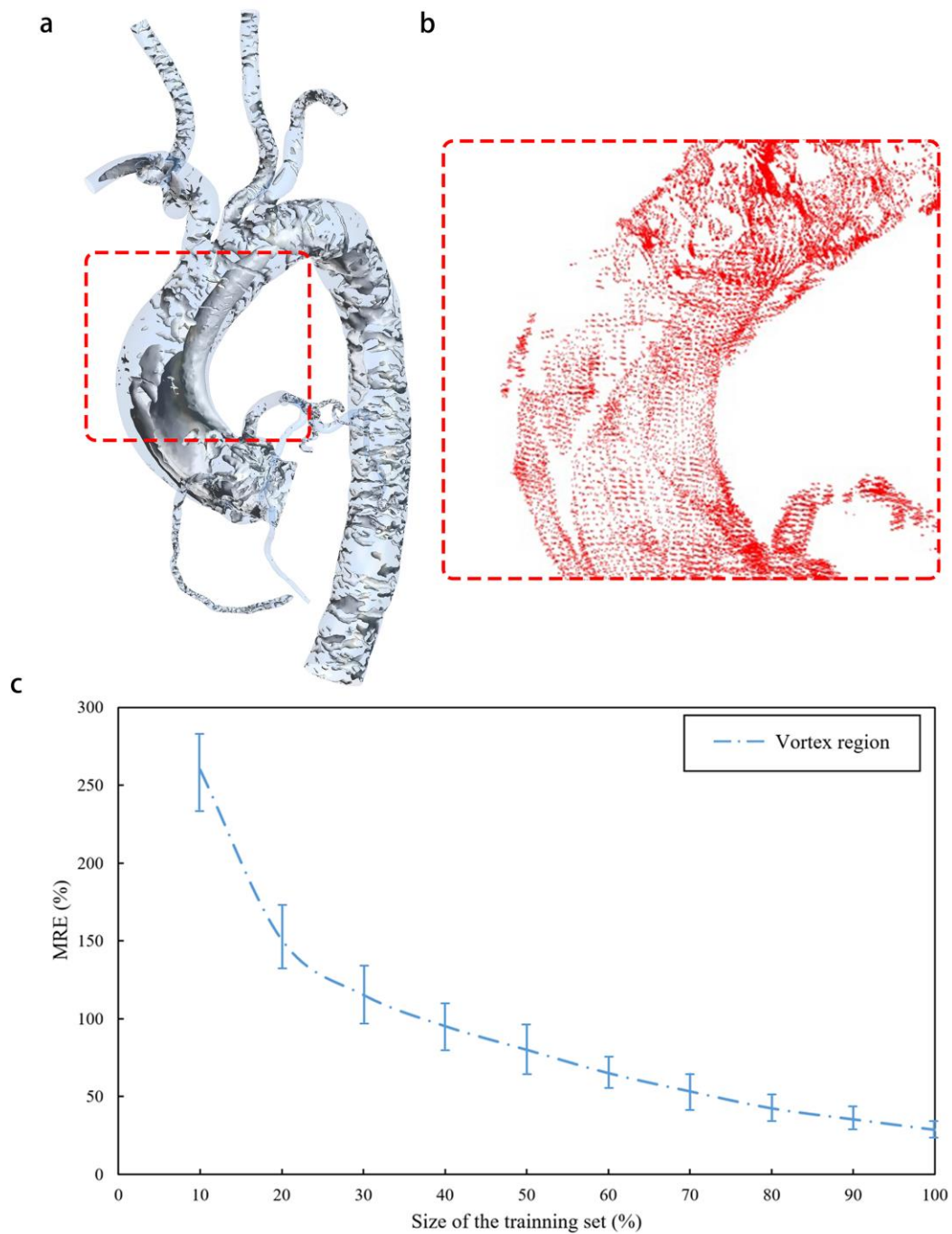
**Fig. 4** Prediction error analysis. Using a model in the preoperative test set as a sample, **a** shows the vortex regions in its CFD simulation flow field, which are mostly distributed in the aorta and superior aortic branch artery rather than the grafts and coronary arteries. Compared to the entire model, the number of points in the vortex region of grafts and coronary arteries only accounted for 0.1% of all query points. For most models, there is an obvious vortex region in the ascending aorta area circled by the red box. In order to clearly indicate the distribution of points with high prediction errors (MRE> 10%), **b** shows the points with high errors in deep learning predicted velocity field of the same model as **a** (the circled area). The distribution of these points is highly consistent with the vortex region in **a**, which proves that the error mainly comes from the vortex region of the aorta and superior aortic branch artery. **c** shows the prediction errors along to the different size of training set only in the vortex region. **c** shows the influence of the training set size on MRE of the vortex region. We fix the test set and increase the size of the training set from 10% to 100%. Then we calculate and observe the MRE of the vortex region. When the size of the training set reach 100%, MRE still displays a downward trend. The minimum value of 28.53% is still far greater than the aorta and superior aortic branch artery MRE of 9.74±3.83% as shown in Table 1. It further confirms the source of the prediction error and shows that it is necessary to increase the size of training sets.

Compared to laminar flow, the vortex flow part was extremely complicated. Previous studies that used deep learning to predict complex vortexes required much more training data than ours, even in 2D space[39-41]. Taking Lee's research as an example[39], in a 2D plane with a size of 250×250 (grid cells), 500,000 vortex samples were needed to train the network. The number of samples was far more than that of this study. However, the complexity of the vortex (2D) was lower than that of this study (3D). Therefore, we hypothesized that the limited dataset of this study was not sufficient to fully characterize the characteristics of vortex, which could lead to a decrease in the accuracy of the prediction results. To verify this theory, we fixed the test set and increased the size of the training set from 10% to 100% and then calculate the MRE of the vortex region, as shown in Fig. 4c. Even at the maximum of the training set, the MRE of the vortex part still had a downward trend. With a larger dataset, accuracy would also improve. The collection of more cardiovascular models of patients with coronary artery stenosis to build a richer dataset is necessary as more data will lead to higher prediction accuracy and better model performance.

# Discussion

In this study, we used deep learning to predict 3D hemodynamics of complex cardiovascular systems with small grafts and coronary branches before and after CABG surgery. Our results showed that calculation results of the deep learning and CFD methods were highly consistent, and the calculation efficiency was improved 600-fold. This study proved that deep learning could achieve efficient and accurate predictions of 3D hemodynamics in complex models, which also means that it has great application value in scientific research and clinical fields.

The comparative analysis of our deep learning method against previous deep learning approaches is available in the Supplementary Table 1. As mentioned above, there was no previous research that achieved 3D hemodynamic prediction of complex models such as thoracic aortic tree including the small grafts and coronary branches. Our work made up for this gap, which was mainly due to the use of the point cloud to create datasets and propose a high-performance deep learning network. Previous studies typically required normalized flow field data to help deep learning networks obtain correspondence between model geometry and flow field distribution[24,25]. In other words, regular spatial relationships (e.g., orthogonalization) are introduced into the flow field data by interpolation or other methods. Therefore, the spatial resolution of flow field data depends on space segmentation size during normalization. When there are big differences in the size of different parts of the model, such as the radius of the aorta which is much larger than that of the coronary artery and the graft in this study, it will be very difficult to choose the appropriate space segmentation size. Large segmentation sizes cannot characterize small parts of the model. Small segmentation size results in a large amount of data exceeded the upper limit of server processing. For example, when using Guo et al's normalization method to process the cardiovascular models in this study[28], we should place the model in a three-dimensional space cuboid. The length, width and height of the cuboid should be the maximum value in the corresponding direction of the model. For a cardiovascular model with a length of 80 mm, a width of 120 mm and a height of 95 mm, when using 0.1 mm as the segmentation size, one 3D cardiovascular model needs to have $800 \times 1200 \times 950 = 836,000,000$ normalized points to contain the mean shape, which is unacceptable for network and GPU processors. Liang et al. proposed a normalization method for deep learning[29]. However, it was only suitable for large ideal aorta, not for the whole complex cardiovascular system, especially for small coronary branches. In addition, Liang et al. normalized the thoracic aortic models of different patients to the same meshes with only 80100 nodes. However, in this study, the mesh independence test (as seen in the

Supplementary Methods) showed that for the thoracic aortic, when the number of meshes exceeded one million, the CFD simulation results can be considered to be stable. Therefore, the deep learning method proposed by Liang et al. still has great limitations in the application range and data resolution. Due to limitations of resolution and network performance, most of the previous research objects are simple idealized flow fields. Unlike previous approaches, we utilized high-density 3D point clouds to build datasets. A point cloud is the connection point of CFD meshes and is generally called a node. It is directly output by the mesh result and does not require normalization or other processing. The point cloud can represent complex or small features of the model under the appropriate mesh setting[42,43]. In this study, the mesh independence test results (as seen in the Supplementary Methods) confirmed that the model contains about 2 million points that could represent the complex structure of the entire cardiovascular system, of which 0.4 million were surface model point clouds and 1.6 million were internal query point clouds. Each point has only spatial coordinates and hemodynamic information, which means there is no connection or interaction between them. Thus, it can store a lot of useful information with a small amount of data unlike a connected point set. In order to resolve the disorder of the point cloud and introduce the spatial relationship, we propose a dual sampling channel network structure based on PointNet. Since there is no connectivity information between the points, there is no specific input sequence for the points. That is to say, when N points are used as input to the network, due to the different input sequence, there may be N! input permutations, that is, the disorder of the point cloud. Symmetric function can ensure that the output is the same regardless of the order of input, to resolve point disorder[37]. The dual sampling channel can extract the geometry of the model point cloud of the surface as the global geometry feature, and the internal query point cloud distribution as the local flow field feature. Global features convey the outer geometry information within the model, which can help the query point cloud to obtain its position inside the model. Under the uniform CFD boundary conditions, the position of the query point is corresponding to the flow field. The local flow field characteristics and the corresponding position information can be used as teacher signals to help the network learn the hemodynamic values of a specific position. In this way, the spatial relationship is effectively introduced to help the network attain correspondence between the model geometry and the flow field distribution.

Our deep learning method is highly universal, which is not limited to guiding the implementation of CABG and the treatment of CHD. It can analyze and reproduce the relationship between complex cardiovascular geometry and hemodynamics in a given dataset, which can be extended to the hemodynamic simulation of other organs and tissues, or even the flow field research under

experimental conditions, such as replacing the steady flow 3D PIV experiment with sufficient data. From a technical perspective, our deep learning method is highly practical. For different properties of hemodynamic parameters, the prediction can still be completed without adjusting the network structure, which was difficult to achieve in the past[28,29]. The analysis results of the velocity and pressure fields confirm that the same network structure can achieve high accuracy predictions for physical fields with and without spatial components. In addition, point cloud, as a conventional data format, can be accepted by most of analysis software (e.g., ANSYS and Python) which makes the processing of point cloud data relatively easy. In terms of resolution, universality, accuracy and computational efficiency, our deep learning method can meet the needs of most situations. We also noticed that the four data sets (preoperative, postoperative, velocity, and pressure fields) need to be trained separately as inputs, which increased the computational cost and operational complexity of deep learning to a certain extent. Therefore, we will explore potential improvements due to similarities in features between the different fields and application scenarios in further work. For example, by merging four data sets (with different labels), all prediction results can be output in one training session.

The biggest limitation of this study is the lack of clinical data. In CFD simulation, there is no boundary condition information for patients. Currently we adopted constant values on inlets and outlets, which have been widely used among a number of geometries[44-46]. Therefore, the simulation results should include differences from real hemodynamics. In future approaches that include boundary conditions, another input channel will be required on the network. This input channel will take the patient's personalized boundary conditions as the input, and together with the model point cloud as the teaching signal to control the training process. In the analysis of prediction accuracy, we only compared the prediction results of deep learning with CFD, but lack of comparison with clinically measured data of patients (such as invasive FFR). Itu et al.[47] and Tesche et al.[48] proved that under the premise of good consistency between the FFR calculated by deep learning and CFD, compared with the invasive FFR, the FFR values calculated by these three methods were also with good consistency, which we intend to address in the future. The data for this study comes from a project optimizing the treatment plan of coronary stenosis. Therefore, our datasets do not contain information on other cardiovascular diseases such as coronary aneurysms or aortic diseases. In addition, the point cloud data used in this study is extracted from the CFD meshing result. In the point cloud extraction process, we deleted the connection relationship between the grids. Although the point cloud can reproduce the CFD flow field prediction results, it also brings potential

limitations, such as the loss of correlation information between different nodes in the original CFD results and the introduction of the disorder of point clouds. Based on the above limitations and prediction error analysis results, in future work, we need to increase the number and type of patients in datasets to include the characteristics of different cardiovascular diseases and improve the accuracy of predictions. Regarding the datasets with several types of disease, we also need to establish the quantitative methodology to evaluate the variety of geometry as a training data. Secondly, we need to collect physiological information of patients to build the datasets under personalized boundary conditions. Based on this study, we aim to build a network with multiple constraints, multiple channels of input, and multiple sampling layers in parallel. It can help us use deep learning to achieve the prediction of high-dimensional flow field such as fluid–structure interaction (FSI), etc. Thirdly, the uncertainty of vessel wall identification should be noted as the common limitation in image-based analysis including CFD. Present study exhibits the flow estimation on the point clouds which generated on segmented blood vessel. Then, the flow field strongly depends on the quality of vessel wall segmentation. Though CFD results from the same STL file can exhibit good consistency among different research groups[49], still segmentation process from DICOM images can lead to variability in geometry[50]. To overcome this uncertainty of real geometry, the establishment of stable segmentation method or normalization of hemodynamic parameters will be required.

## Methods

### Ethics approvals

The experimental scheme and related details of this study were approved by the Institutional Ethics Committee of People's Hospital (Beijing, China) and Tohoku University (Sendai, Miyagi, Japan). All experiments were carried out in accordance with relevant guidelines and regulations. We explained research content to the subjects in detail and obtained their written informed consent.

### Data collection

The patient data used in this study was based on the project 'Biomechanics study on quantitative relationships between coronary artery stenosis and myocardial ischemia[51-53], which focused on the diagnosis and optimization of coronary stenosis surgical procedures. The CTA data for 110 patients with LAD stenosis who had visited the People's hospital since 2018 was collected and collated by professional clinicians with a 128-slice CT scanner (Brilliance iCT, Philips Healthcare, The

Netherlands). 3D model reconstruction was also performed by the clinician. We obtained 110 STL cardiovascular models as raw data.

**Model geometric parameters modification**

The deep learning dataset, which only contained 110 real cardiovascular models, had a very limited amount of information, which was far from enough to represent the relationship between the geometry of the model and the corresponding hemodynamics. Therefore, based on the statistical results of previous cardiovascular morphology studies[47,48,54-59], the geometric parameters of the 110 original cardiovascular models were adjusted to increase the number of models. For each parameter, we randomly selected one value within the given range as the modification basis of the original model, as shown in Table 3. Based on this method, we extended one original model into nine new models, which meant that the total number of models increased to 1100, as shown in Supplementary Fig. 2.

Table 3. Geometric parameters with corresponding ranges

| | Geometric parameter | Parameter details or measurement methods | Range |
|---|---|---|---|
| Coronary artery | Number of branches[47,48] | Main branches | 3 (LAD, LCX, RC) |
| | | Side branches | 0 - 3 |
| | Bifurcation angle between LAD and LCX[54,55] | The angle described by the two branches in the first 10 mm of their course was measured | 30-90° |
| | Stenosis location | Random positions on LAD | LAD(main branch) |
| | Number of stenosis | Determined by the patient's actual condition | 1-2 |
| | Stenosis Rate | Idealized stenosis model | 60-90% |
| Aorta and superior aortic branch artery | Aortic arch angulation[56,57] | Angulation of the arch at the level of the left subclavian artery | 80-140° |
| | Diameter of ascending aorta[58,59] | Increased or decreased the diameter of original artery uniformly | 20-30mm |
| | Diameter of descending aorta[58,59] | Increased or decreased the diameter of original artery uniformly | 15-20mm |
| | Superior aortic branch artery | Kept the original geometry | |

**Simulated operation of CABG and CFD simulation**

After model expansion, we performed the simulation implementation of the CABG operation and the CFD simulation.

As the most patients did not have undergone CABG surgery, the virtual bypass surgery was performed except for undergone CABG case. With the agreements of clinicians, the left internal mammary artery (LIMA) with diameter of 2 mm was deployed using modeling software Mimics (Materialize NV, BE).

According to the generation of geometry, tetrahedron numerical meshes with boundary layers were generated by ANSYS-Meshing (ANSYS, Canonsburg, USA). Total mesh number was selected to have the number of nodes from 2.83 to 3.01 million based on mesh-independence test.

Steady flow simulation was performed on ANSYS-CFX (ANSYS, Canonsburg, USA). Blood flow was simplified to be an incompressible Newtonian fluid with 1050 kg/m$^3$ density and 0.0035 Pa·s viscosity. Velocity boundary of 1.125 m/s was imposed on the inlet assuming the peak wave velocity of cardiac cycle[60]. Outlet boundary was set as zero pressure condition. No-slip condition was assigned to all wall boundaries.

More detail is summarized in the Supplementary Method.

**Creation of datasets and proposal of deep learning network**

Using simulation software (e.g., ANSYS, OpenFOAM, etc.), the high-density 3D point cloud form of the four groups—preoperative, postoperative, velocity, and pressure fields— of the CFD simulation results could be directly output (i.e., they could be represented as a set of points {$Pi$ | $i$ = 1, ..., N} in space). Each point $Pi$ was a vector containing spatial coordinates (x, y, z) and hemodynamic parameters at that point. $Pi$ was the connection point of CFD meshes (usually called node). CFD meshes generation was only related to the geometry of the model. Therefore, the distribution of points depended only on the geometry of the model. The position of points in the model was fixed, we could not change its spatial distribution. What we could do is to directly extract and analyze the points in a certain position through the simulation software.

We divided each group of point cloud data into two sets: a training set and a test set. The training set included simulation results of 1000 cardiovascular models based on the original 100 models. In order to ensure the generalization of the deep learning network, the test set consisted of the CFD results of 100 cardiovascular models that were expanded from the 10 original models which were different from the training set. Based on this, the four groups—preoperative, postoperative, velocity, and pressure fields— of hemodynamic datasets were established, respectively. These four datasets were used independently to train four separate networks. Hence, we obtain four optimal network configurations to further predict the corresponding hemodynamics.

In the case of certain boundary conditions, the values of flow velocity and pressure at each point were jointly determined by the overall shape of the model and its specific spatial coordinates. This was also the basic principle for CFD to resolve the simulation results via the Navier-Stokes and continuity equations. The segmentation network structure of PointNet[37] could realize feature extraction and hemodynamic prediction of point clouds. This study inherited the concepts of global feature and local feature proposed by the original PointNet, and optimized the network structure. Since the original PointNet had only one single input channel, global features and local features were extracted from the same and all input points, which could help the PointNet identify the relationship between these two features. However, it was inevitable that there would be duplication between the two features, and then some effective and specific information would be lost. In order to solve this problem, a network structure with double input and double sampling channels was proposed in this study. The structure and parameter setting were shown in Fig. 5. For each model in the dataset, we extracted two types of point clouds. One was the model point cloud, which only included spatial coordinates for the outermost points of the cardiovascular model. These points could represent the global features of the overall model geometry. The second was the query point cloud, which included the remaining points inside the cardiovascular model. These points contained local features such as the spatial coordinates of each point and its corresponding hemodynamics. The 3D deep learning network had two independent input channels that corresponded to these two point clouds. Two feature extraction parts were directly connected to their respective input and sampling channels. This effectively enhanced the extraction of effective and specific information from these two features, and improved the prediction accuracy. For the same point cloud data, the comparison of prediction MRE from the original single channel PointNet and our dual channel network was shown in Table 4. The prediction ERR of our dual channel network was lower than that of the original PointNet.

Table 4. Comparison of MRE from original PointNet and our network *

| Hemodynamic | Velocity field | Pressure field |
|---|---|---|
| Original PointNet | 18.42±6.71 | 14.59±5.31 |
| Our Network | 9.77±3.86 | 7.61±1.99 |

* The MRE is calculated according to the hemodynamic prediction values of preoperative aorta and superior aortic branch artery.
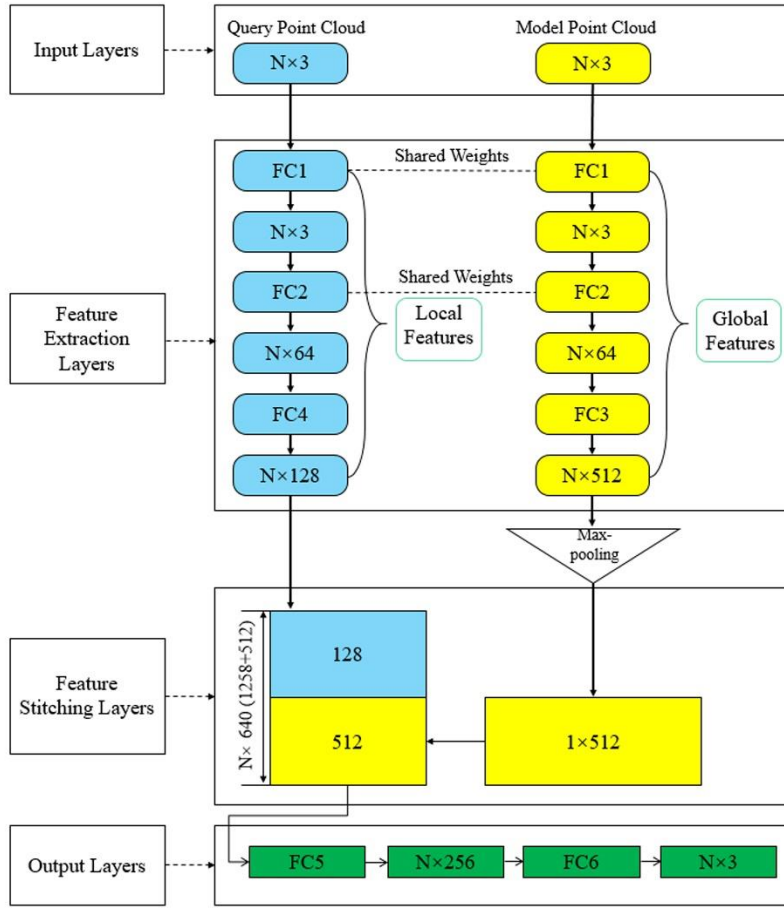
**Fig. 5** Deep learning network construction. The network takes N points with three-dimensional spatial components of x, y, and z (for pressure, the three component values are the same) as input. After feature extraction and stitching layer processing, spatial relationships are introduced to extract and reproduce the relationship between model geometry and hemodynamic. The Maxpooling layer resolves the disorder of the point cloud. The output of the network is the hemodynamic three-dimensional spatial components of N points in corresponding query point cloud.

Global features were the global geometric information of the model. Local features referred to the location of each point and the corresponding flow field distribution inside the model. These two features both contained the geometric features of the same cardiovascular model (commonality). The two features also had different effective information (difference). The network needed to extract commonality and difference and learned the correlation between them to further realize the flow field prediction.

Based on the above principle, the network construction scheme was as follows:

To enhance the commonality and correlation, the first two feedforward fully-connected layers (FC1 and FC2) of the two feature extraction sections shared weights, which meant they shared the same underlying feature extraction methods. In order to evaluate the necessity of sharing weights, we compared the network without shared weights with the results of this study, as shown in Table 5. The results showed that the shared weight could effectively reduce the prediction error. The two feature extraction sections also had independent feedforward fully-connected layers (FC3 and FC4), which further enhanced the ability of the network to recognize the effective and specific information (difference) of global features and local features. After FC3 and FC4, the global and local features contained in the two point clouds were represented as a N * 512 and N * 128-dimensional vectors, respectively. We concatenated the two vectors to form an N * 640-dimensional vector. This vector contained both the global features of the model point cloud and the local features of the query point cloud, which helped the network further integrate the correlation between the two features. The last part of the network was feedforward fully-connected layers (FC5 and FC6), which were used to yield hemodynamic results.

Table 5. Comparison of MRE from network with or without shared weights*

| Hemodynamic | Velocity field | Pressure field |
|---|---|---|
| Without shared weights | 16.37±5.43 | 13.42±5.21 |
| With shared weights | 9.77±3.86 | 7.61±1.99 |

* The MRE is calculated according to the hemodynamic prediction values of preoperative aorta and superior aortic branch artery.

For other details of the network, we added a Maxpooling layer as a symmetric function in the feature extraction part of the model point cloud, which could aid in resolving the disorder of the input point cloud[37]. We used the mean absolute error as the regression loss function[24,61]. We used the Adam optimizer with specific parameters: learning rate = 0.001, $\epsilon$ = 0.001, $\rho 1$ = 0.9, $\rho 2$ = 0.999, and $\delta$ = 1E−8[62]. The 3D deep learning network was trained by TensorFlow (v2.0.0rc, Python 3.6 on a Nvidia GeForce GTX 1080 Ti GPU). The preoperative and postoperative datasets needed to be separately trained as inputs for the network. During the training process, we saved the optimal network parameter configurations for both training sets. After that, while only inputting the spatial coordinates in the test set, the network could recognize the hemodynamic prediction output of query point cloud.

**Definition of error functions**

Referring to the evaluation criteria of previous studies, NMAE[29] and MRE[28] were defined as error functions to evaluate the accuracy of deep learning network predictions based on the CFD results, as shown in equation (1) and equation (2):

$$\text{NMAE} = \frac{1}{N} \frac{\sum_{i=1}^{N} |P_i - \hat{P}_i|}{\text{Max}|P| - \text{Min}|P|} \times 100\% \tag{1}$$

$$\text{MRE} = \frac{1}{N} \sum_{i=1}^{N} \frac{\sqrt{(P_i - \hat{P}_i)^2}}{\sqrt{P_i^2}} \times 100\% \tag{2}$$

*N* represented the number of selected query points. *i* was the spatial sequence of the 3D point cloud. *Pi* and $\hat{P}_i$ represented the flow velocity or pressure value at a certain point calculated by CFD and deep learning, respectively. $\text{Max}|P|$ and $\text{Min}|P|$ represented the maximum and minimum magnitude of the corresponding hemodynamic parameters among all points in the selected area, respectively. NMAE can characterize the error of the deep learning prediction result relative to the true value of the overall flow field (CFD result). MRE can characterize the error of the deep learning prediction value relative to the true value at all query points of the model. The definition of the error function draws on previous studies. The comparative analysis results are shown in Supplementary Table 1. In this study, ERR is designed to evaluate the velocity or pressure fields represented by point clouds. For other parameters (such as FFR calculated by pressure field, etc.), new ERR should be defined according to the specific situation. In these definitions, each of the points of different cardiovascular parts can affect ERR with the same weight. However, the number of points and the magnitude of velocity and pressure must have a great difference among aorta, coronary arteries, and bypass graft. In order to avoid the impact of this variation on the evaluation results, local ERR (The model was divided into several parts, and the ERR value of a certain part, such as the left anterior descending branch, was called local ERR.) values were obtained to assess the prediction accuracy on small-to-large parts. We calculated the ERR values of the proximal and distal end of left anterior descending artery (LAD), graft, right coronary artery (RA), the left circumflex branch (LCX), the aorta and superior aortic branch artery, respectively. Regarding the LAD, the proximal and distal ends were divided by stenosis. When there were multiple stenosis in the LAD branch, the stenosis with highest degree was selected.

**Statistics and reproducibility**

All ERR calculations were based on the velocity or pressure results of 100 models in the test set. The definition of query point cloud number ($i$) was defined in equation (1) and equation (2). This study took the average value of ERR of 100 models. The standard deviation was used to calculate the error bars.

**Data availability**

Data analyzed during the current study are available from the corresponding author upon reasonable request. Restrictions apply to the sharing of patient data that supports the findings of this study. With the approval of the Institutional Ethics Committee of People's Hospital, the patient's data can be authorized for use by qualified researchers.

**Code availability**

All source code described in this project can be accessed at: https://doi.org/10.5281/zenodo.4287103

# References

1. Wallace, D. & Wallace, R. Early Mortality from Ischemic Heart Disease (Coronary Heart Disease). in *Right-to-Work Laws and the Crumbling of American Public Health* 61–69 (2018).

2. Tuppo, E. *et al.* Changes in coronary heart disease incidence and mortality in New Jersey 2000-2017. https://doi.org/doi:10.7282/t3-fzmb-8d61 (2019).

3. Maddox, T. M. *et al.* Nonobstructive coronary artery disease and risk of myocardial infarction. *JAMA - J. Am. Med. Assoc.* **312,** 1754-1763 (2014).

4. Saka, Y. *et al.* Clinical comparison study between a newly developed optical-based fractional flow reserve device and the conventional fractional flow reserve device. *Coron. Artery Dis.* **Publish Ahead of Print**, (2020).

5. Wong, C. *et al.* Validation of a Novel 'Wireless' Fractional Flow Reserve Measurement During Coronary Angiography. *Hear. Lung Circ.* **27**, S487 (2018).

6. Wang, W. *et al.* A Fast-Fractional Flow Reserve Simulation Method in A Patient with Coronary Stenosis Based on Resistance Boundary Conditions. *Comput. Model. Eng. Sci.* **116**, 163–173 (2018).

7. Yue Feng, Y. L. Study on the Influence of Right Atrial Pressure on the Numerical Calculation of Fractional Flow Reserve. *Mol. Cell. Biomech.* **16**, 31–32 (2019).

8. Zhang, Z., Li, K. & Tian, J. Efficacy and safety outcomes of fractional flow reserve in guiding clinical therapy of non-ST-segment elevation myocardial infarction compared with angiography alone in elderly Chinese patients. *Clin. Interv. Aging.* **11**, 1751–1754 (2016).

9. Shin, J. *et al.* Fractional Flow Reserve Guided Coronary Revascularization in Lung Transplant Recipients. *J. Hear. Lung Transplant.* **38**, S323 (2019).

10. Squiers, J. J. & Mack, M. J. Coronary artery bypass grafting-fifty years of quality initiatives since Favaloro. *Ann. Cardiothorac. Surg.* **7**, 516–520 (2018).

11. Amin, S., Werner, R. S., Madsen, P. L., Krasopoulos, G. & Taggart, D. P. Intraoperative Bypass Graft Flow Measurement With Transit Time Flowmetry: A Clinical Assessment. *Ann. Thorac. Surg.* **106**, 532–538 (2018).

12. Handa, T., Orihashi, K., Nishimori, H. & Yamamoto, M. Maximal blood flow acceleration analysis in the early diastolic phase for aortocoronary artery bypass grafts: a new transit-time flow measurement predictor of graft failure following coronary artery bypass grafting. *Surg. Today* **46**, 1325–1333 (2016).

13. Zhuang, B., Wang, S., Zhao, S. & Lu, M. Computed tomography angiography-derived fractional flow reserve (CT-FFR) for the detection of myocardial ischemia with invasive fractional flow reserve as reference: systematic review and meta-analysis. *Eur. Radiol.* **30**, 712–725 (2020).

14. Westra, J. *et al.* Diagnostic performance of in-procedure angiography-derived quantitative flow reserve compared to pressure-derived fractional flow reserve: the FAVOR II Europe-Japan study. *J. Am. Heart Assoc.* **7**, e009603 (2018).

15. Zhang, M. *et al.* Haemodynamic effects of stent diameter and compaction ratio on flow-diversion treatment of intracranial aneurysms: a numerical study of a successful and an unsuccessful case. *J. Biomech.* **58**, 179–186 (2017).

16. Zhang, M., Anzai, H., Chopard, B. & Ohta, M. Towards the patient-specific design of flow diverters made from helix-like wires: an optimization study. *Biomed. Eng. Online* **15**, 159 (2016).

17. Hoi, Y. et al. Effects of arterial geometry on aneurysm growth: three-dimensional computational fluid dynamics study. *Journal of neurosurgery.* **101,** 676-681 (2004).

18. Qiao, A., Liu, Y., Li, S. & Zhao, H. Numerical simulation of physiological blood flow in 2-way coronary artery bypass grafts. *J. Biol. Phys.* **31**, 161–182 (2005).

19. Fu, Y., Qiao, A., Yang, Y. & Fan, X. Numerical Simulation of the Effect of Pulmonary Vascular Resistance on the Hemodynamics of Reoperation after Failure of One and a Half Ventricle Repair. *Front. Physiol.* **11**, 207 (2020).

20. Taylor, C. A., Fonte, T. A. & Min, J. K. Computational Fluid Dynamics Applied to Cardiac Computed Tomography for Noninvasive Quantification of Fractional Flow Reserve : Scientific Basis. *J. Am. Coll. Cardiol.* **61**, 2233–2241 (2013).

21. Li, G. *et al.* Pulse-Wave-Pattern Classification with a Convolutional Neural Network. *Sci. Rep.* **9**, 1–11 (2019).

22. Huang, G. B., Lee, H. & Learned-Miller, E. Learning hierarchical representations for face verification with convolutional deep belief networks. *2012 IEEE Conference on Computer Vision and Pattern Recognition.* 2518–2525 (2012).

23. Simonyan, K. & Zisserman, A. Very Deep Convolutional Networks for Large-Scale Image Recognition. *arXiv:1409.1556* (2014).

24. Jha, D. *et al.* Enhancing materials property prediction by leveraging computational and experimental data using deep transfer learning. *Nat. Commun.* **10**, 1–12 (2019).

25. Varadarajan, A. V *et al.* Predicting optical coherence tomography-derived diabetic macular edema grades from fundus photographs using deep learning. *Nat. Commun.* **11**, 1–8 (2020).

26. Coenen, A. *et al.* Diagnostic accuracy of a machine-learning approach to coronary computed tomographic angiography–based fractional flow reserve: result from the MACHINE consortium. *Circ. Cardiovasc. Imaging* **11**, e007217 (2018).

27. Wang, Z.-Q. *et al.* Diagnostic accuracy of a deep learning approach to calculate FFR from coronary CT angiography. *J. Geriatr. Cardiol. JGC* **16**, 42 (2019).

28. Guo, X., Li, W. & Iorio, F. Convolutional neural networks for steady flow approximation. In *Proceedings of the 22nd ACM SIGKDD international conference on knowledge discovery and data mining*, 481–490 (2016).

29. Liang, L., Mao, W. & Sun, W. A feasibility study of deep learning for predicting hemodynamics of human thoracic aorta. *J. Biomech.* **99**, 109544 (2020).

30. Kutz, J. N. Deep learning in fluid dynamics. *J. Fluid Mech.* **814**, 1–4 (2017).

31. Miyanawala, T. P. & Jaiman, R. K. An efficient deep learning technique for the Navier-Stokes equations: Application to unsteady wake flow dynamics. *arXiv:1710.09099* (2017).

32. Wang, Z. *et al.* Model identification of reduced order fluid dynamics systems using deep learning. *Int. J. Numer. Methods Fluids* **86**, 255–268 (2018).

33. Lye, K. O., Mishra, S. & Ray, D. Deep learning observables in computational fluid dynamics. *J. Comput. Phys.* **401,** 109339 (2020).

34. Lee, S. & You, D. Prediction of laminar vortex shedding over a cylinder using deep learning. *arXiv:1712.07854* (2017).

35. Graham, L. N., Ellison, K., Herman, B. K. & Riddell, C. S. Visualization and storage algorithms associated with processing point cloud data. (2010).

36. You, H., Feng, Y., Ji, R. & Gao, Y. Pvnet: A joint convolutional network of point cloud and multi-view

for 3d shape recognition. in *Proceedings of the 26th ACM international conference on Multimedia* 1310–1318 (2018).

37.  Qi, C. R., Su, H., Mo, K. & Guibas, L. J. Pointnet: Deep learning on point sets for 3d classification and segmentation. in *Proceedings of the IEEE conference on computer vision and pattern recognition* 652–660 (2017).

38.  Pijls, N. H. *et al.* Measurement of fractional flow reserve to assess the functional severity of coronary-artery stenoses. *N. Engl. J. Med.* **334**, 1703 (1996).

39.  Lee, S. & You, D. Data-driven prediction of unsteady flow over a circular cylinder using deep learning. *J. Fluid Mech.* **879**, 217–254 (2019).

40.  Duriez, T., Brunton, S. L. & Noack, B. R. *Machine learning control-taming nonlinear dynamics and turbulence Ch. 6* (Springer, Cham. Press, Switzerland, 2017).

41.  Ling, J., Kurzawski, A. & Templeton, J. Reynolds averaged turbulence modelling using deep neural networks with embedded invariance. *J. Fluid Mech.* **807**, 155–166 (2016).

42.  Layton, W. & Lenferink, H. W. J. A multilevel mesh independence principle for the Navier–Stokes equations. *SIAM J. Numer. Anal.* **33**, 17–30 (1996).

43.  Frey, P.J. & Alauzet, F. Anisotropic mesh adaptation for CFD computations. *Comput. Methods Appl. Mech. Eng.* **194**, 5068–5082 (2005).

44.  Boutsianis, E. *et al.* CFD and PTV Steady Flow Investigation in an Anatomically Accurate Abdominal Aortic Aneurysm. *J. Biomech. Eng.* **131**, 011008-011023 (2008).

45.  Vinoth, R. *et al.* Steady and Transient Flow CFD Simulations in an Aorta Model of Normal and Aortic Aneurysm Subjects. in *The Proceedings of the International Conference on Sensing and Imaging.* 29–43 (2019).

46.  Martin, J. D. CFD Analysis Comparing Steady Flow and Pulsatile Flow Through the Aorta and its Main Branches. *ASME 2016 International Mechanical Engineering Congress and Exposition.* **3,** IMECE2016-67155, V003T04A064 (2016)

47.  Itu, L. *et al.* A machine-learning approach for computation of fractional flow reserve from coronary computed tomography. *J. Appl. Physiol.* **121**, 42–52 (2016).

48.  Tesche, C. *et al.* Coronary CT angiography–derived fractional flow reserve: machine learning algorithm

versus computational fluid dynamics modeling. *Radiology* **288**, 64–72 (2018).

49. Radaelli, A. G. *et al.* Reproducibility of haemodynamical simulations in a subject-specific stented aneurysm model—a report on the Virtual Intracranial Stenting Challenge 2007. *J. Biomech.* **41**, 2069–2081 (2008).

50. Berg, P. *et al.* Multiple aneurysms anatomy challenge 2018 (MATCH): phase I: segmentation. *Cardiovasc. Eng. Technol.* **9**, 565–581 (2018).

51. Ge, X. *et al.* Model-based analysis of the sensitivities and diagnostic implications of FFR and CFR under various pathological conditions. *Int. j. numer. method. biomed. eng.* https://doi.org/10.1002/cnm.3257 (2019)

52. Li, B., Wang, W., Mao, B. & Liu, Y. A Method to Personalize the Lumped Parameter Model of Coronary Artery. *Int. J. Comput. Methods* **16**, 1842004 (2019).

53. Wang, W. *et al.* Numerical Simulation of Instantaneous Wave-Free Ratio of Stenosed Coronary Artery. *Int. J. Comput. Methods* **16**, 1842009 (2019).

54. Roy, S., Gupta, A., Nanrah, B. K., Verma, M. & Saha, R. Morphometric study of left coronary artery trunk in adult human cadavers: a study on the eastern region population. *J. Clin. diagnostic Res. JCDR* **8**, 7 (2014).

55. Kassab, G. S. & Fung, Y.-C. B. The pattern of coronary arteriolar bifurcations and the uniform shear hypothesis. *Ann. Biomed. Eng.* **23**, 13–20 (1995).

56. Malkawi, A. H. *et al.* Morphology of aortic arch pathology: implications for endovascular repair. *J. Endovasc. Ther.* **17**, 474–479 (2010).

57. Canaud, L. *et al.* Proximal fixation of thoracic stent-grafts as a function of oversizing and increasing aortic arch angulation in human cadaveric aortas. *J. Endovasc. Ther.* **15**, 326–334 (2008).

58. Campens, L. *et al.* Reference values for echocardiographic assessment of the diameter of the aortic root and ascending aorta spanning all age categories. *Am. J. Cardiol.* **114**, 914–920 (2014).

59. Hager, A. *et al.* Diameters of the thoracic aorta throughout life as measured with helical computed tomography. *J. Thorac. Cardiovasc. Surg.* **123**, 1060–1066 (2002).

60. Febina, J., Sikkandar, M. Y. & Sudharsan, N. M. Wall Shear Stress Estimation of Thoracic Aortic Aneurysm Using Computational Fluid Dynamics. *Comput. Math. Methods Med.* (2018). doi:10.1155/2018/7126532

61. Chai, T. & Draxler, R. R. Root mean square error (RMSE) or mean absolute error (MAE)?–Arguments against avoiding RMSE in the literature. *Geosci. Model Dev.* **7**, 1247–1250 (2014).

62. Kingma, D. P. & Ba, J. Adam: A Method for Stochastic Optimization. *Comput. Sci.* https://doi:10.1063/1.4902458(2014).

## Acknowledgements

## Author contributions

G.L., H.W., Y.L., and A.Q. acquired the data. G.L., H.W., M.Z., S.T., A.Q., M.O., Y.L., and H.A. created and designed this study; G.L., H.W., M.Z., S.T., and H.A. performed the experiments and analyzed the data. All of the authors discussed and co-authored the manuscript. The contributions of G.L. and H.W. were equal.

## Competing interests

The authors declare no competing interests.

**Prediction of 3D Cardiovascular Hemodynamics before and after Coronary Artery Bypass Surgery via Deep Learning**

Gaoyang Li et al.

**Supplementary Information**

# Supplementary Results


a
Learning curve of the preoperative velocity field data set


b
Learning curve of the postoperative velocity field data set


c
Learning curve of the preoperative pressure field data set


d
Learning curve of the postoperative pressure field data set
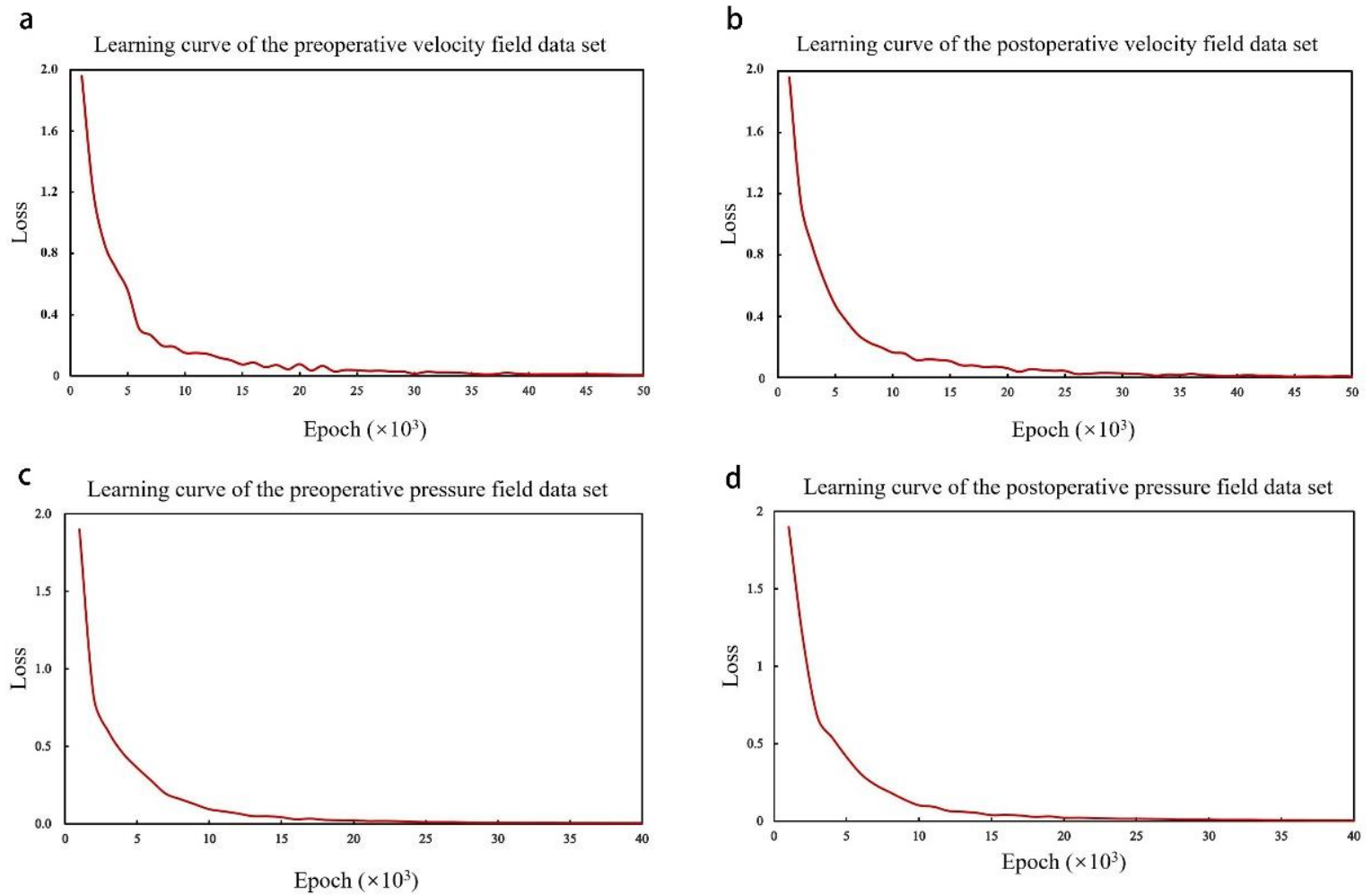
**Supplementary Fig. 1** Learning curve. **a-b** are the learning curves of the pre- and post-velocity field datasets. **c-d** are the learning curves of the pre- and post-pressure field datasets. For velocity, the learning curve reaches a minimum when Epoch is about 50K. For pressure, the learning curve reaches a minimum when Epoch is about 40K.

# Supplementary Discussion

## *Comparison against Previous Deep Learning Approaches*

We reviewed studies using deep learning or machine learning for prediction of flow fields or clinical parameters related to CHD treatment (e.g., FFR), as shown in Supplementary Table 1. Itu's machine learning method was only suitable for the calculation of FFR value[1], and its application range was extremely limited. Lee's convolutional neural network could be used for vortex flow prediction in the 2D plane[2], which might lead to loss of information (such as the flow field component perpendicular to the 2D plane). Guo's deconvolution network is only suitable for 3D regular and simple flow field[3].

Because the network structure is relatively simple, the above studies all need a large number of data samples to support in order to achieve high prediction accuracy. Although Liang realizes the internal hemodynamic prediction of the ideal thoracic aortic model[4], the spatial resolution of its samples is still low, which could not accurately characterize the geometric characteristics of complex cardiovascular system. Liang's network only accepts the input data with prefix array-size. This means, patient geometry should be normalized into template (fixed number of meshes). Then, if the geometry cannot fit into that template, Liang's network cannot accept that input. Under the premise of more extensive information, our deep learning method uses limited data to achieve prediction accuracy similar to previous studies. However, our prediction objects are far more complex. Our network can predict the flow on any kind of geometry owing to using the point cloud format. Even the number of point cloud (nodes) varies, our network can accept that unfixed input. Combined with the universality analysis of the network, our deep learning method has many advantages.

Supplementary Table 1 Comparison analysis of our deep learning method against previous studies

| Network or method | Prediction output | Data set size | Input data format | Error function or accuracy |
|---|---|---|---|---|
| Our Deep Learning Method | 3D Patient Personalized Cardiovascular Hemodynamics | 1100 | High resolution flexible point cloud | NMAE<6.5%, MRE<10% |
| Itu's Machine Learning Approach[1] | FFR Value | 12,000 | Geometric parameters | Accuracy= 99.7% |
| Lee's Adversarial and Convolutional Neural Networks[2] | 2D Vortex Flow | 500000 | Grid cells with fixed number | 32.8%<Error<1% |
| Guo's Deconvolution Network[3] | 3D Regular and Simple Flow | 400000 | Low resolution pixels with fixed number | MRE<3% |
| Liang's DNNs[4] | 3D Ideal Thoracic Aorta Hemodynamics | 729 | Low resolution meshes with fixed number | NMAE<6.5% |

## Supplementary Method

### *Model geometric parameters modification*

In order to visually show the difference between the models in the training set and the test set, and to clearly show the modification of the model's geometric structure, we selected a model from the training

set and the test set, and showed the modification results of its geometric structure, as shown in Supplementary Fig. 2.

## Training set
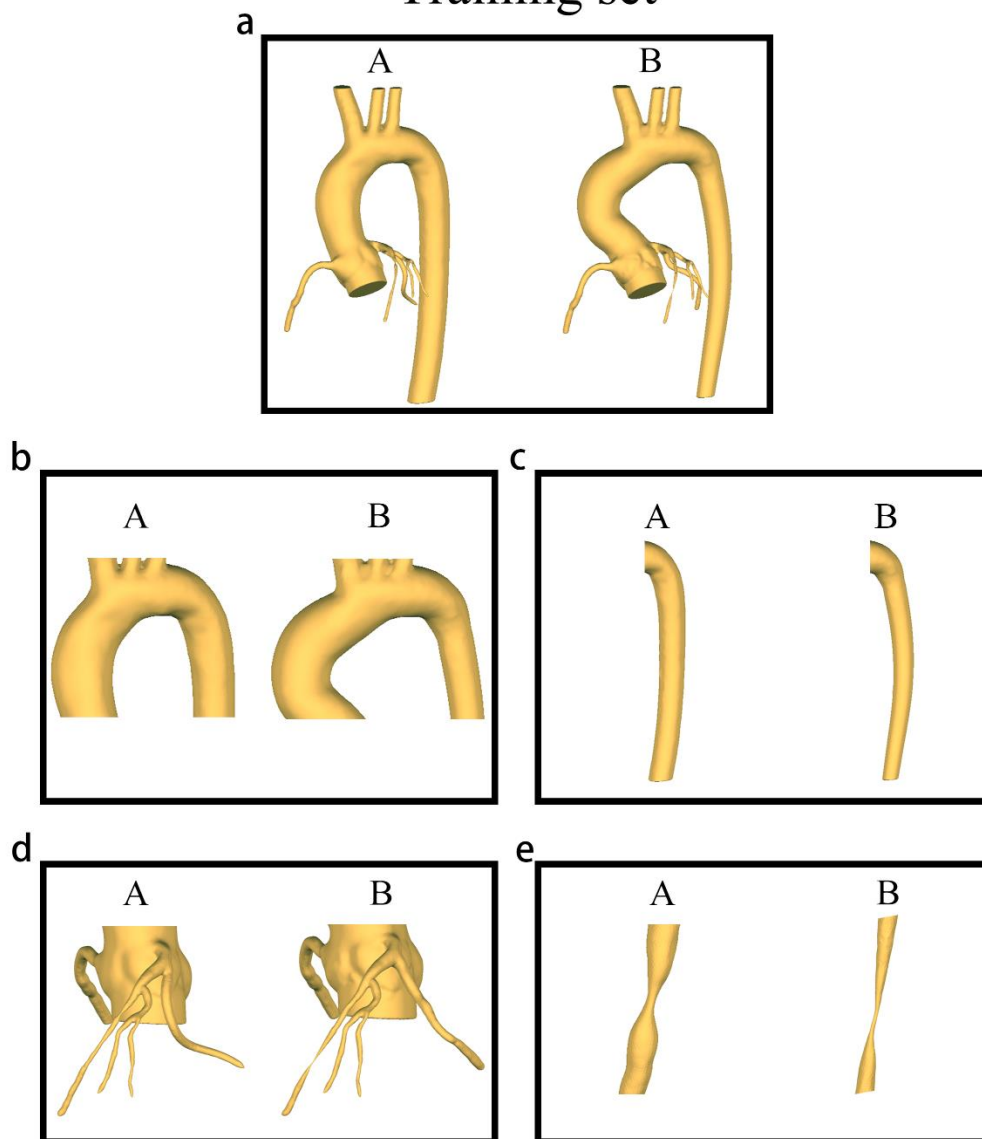
## Test set
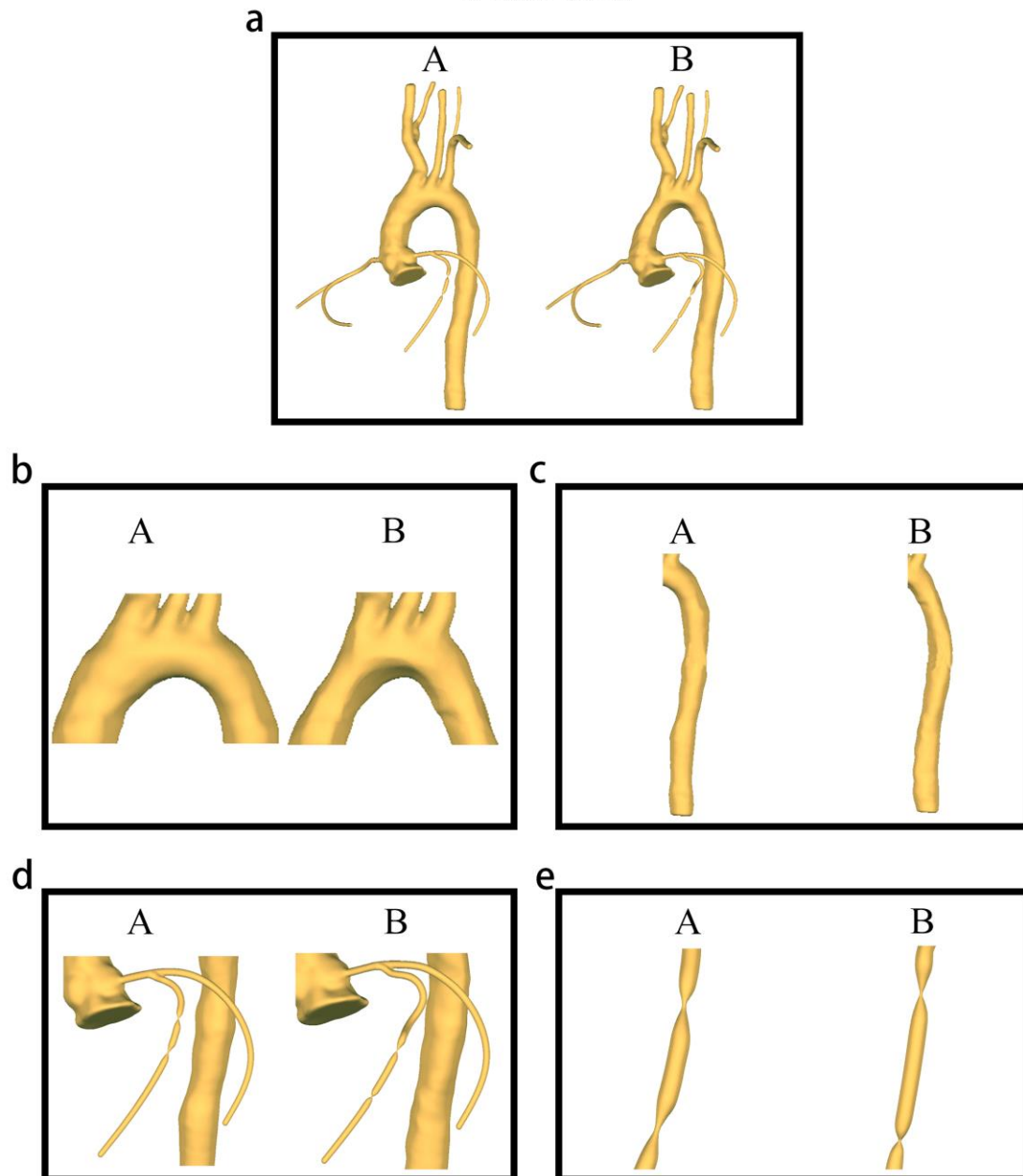


**Supplementary Fig. 2** Examples of models in the training and test sets. Examples of models in the training and test sets. A is the original model. B is the corresponding modified model. **a**: overall model; **b**: ascending aorta and aortic arch angulation; **c**: descending aorta; **d**: coronary artery details (LAD and LCX); **e**: stenosis. All model modifications follow the provisions of Table 3 in the main text.

### Simulated operation of CABG and CFD simulation

Among these patient-specific models, except for a few patients who had undergone CABG surgery, the vast majority of patient data had not undergone CABG surgery. Therefore, virtual CABG bypass surgery was performed on these models. According to the recommendations of existing patients and

doctors, we chose the left internal mammary artery (LIMA) as the bypass graft. The diameter of the blood vessel was 2 mm following the advice of the doctors. In Supplementary Fig. 3, we chose one of the models as an example to show before and after CABG surgery. The operation of virtual surgery was done using the commercially available software Mimics (Materialize NV, BE). Before generating the computational models, the reconstructed 3D models needed to be preprocessed, including surface smoothing and inlet/outlets processing by using the commercially available software Geomagic Wrap (3D system, US). After model preprocessing, tetrahedron-dominant mesh computational models were generated, with maximal sizes of 1.6 mm for the element, for each patient model before and after the CABG procedure using ANSYS-Meshing (ANSYS, Canonsburg, USA). To better capture the flow behaviors, close to the vascular wall, five prismatic boundary layers were generated with a growing ratio of the prism thickness at 1.2 mm[5-8].

The vascular wall was assumed to be rigid and a non-slip condition was assigned at all boundaries. We assumed the blood to be an incompressible Newtonian fluid, with density and viscosity of 1050 kg/m$^3$ and 0.0035 Pa s, respectively, and performed steady flow simulations using solver ANSYS-CFX (ANSYS, Canonsburg, USA). Since the FFR calculation needed to be in the state of maximum congestion, a peak wave velocity of 1.125 m/s was imposed as the boundary condition at the inlet[9]. And for the outlets, a fixed static reference zero pressure was applied. The convergence criteria for simulations were chosen as $10^{-4}$ (Root Mean Square) for the normalized continuity, pressure, and velocity residuals. Upon convergence of each simulation, we extracted four groups of results including preoperative velocity fields and pressure distributions and postoperative velocity fields and pressure distributions and saved them as a CSV file, for further processing and construction of the dataset to be used in deep learning.
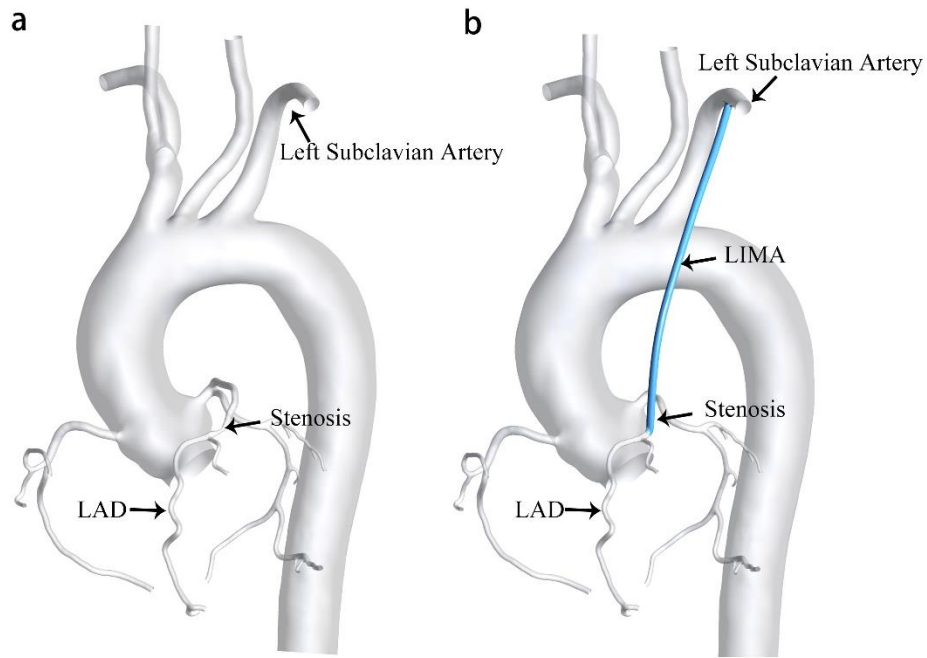
**Supplementary Fig. 3** Simulated operation of CABG.

*Mesh Independence Test*

In this study, the number of nodes ranged from 2.83 to 3.01 million in total across different cases. In order to reduce errors and make the simulation results stable and reliable, a mesh independence test of computational grids was performed. As shown in Supplementary Fig. 4, the relationship between the mass-flow of LIMA and the number of grids. When the number of meshes exceeds one million, the calculation results can be considered to be stable. Therefore, it is confirmed that the number of grids set in this study was appropriate.
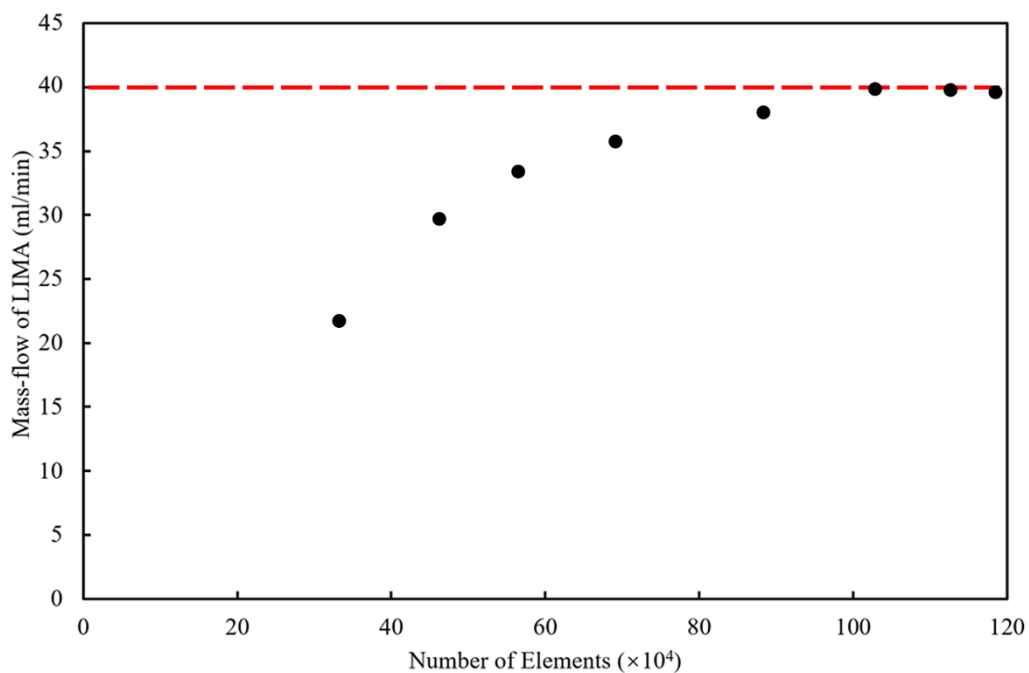
**Supplementary Fig. 4** Mesh independence test. It confirms that the mesh setting of this study is suitable.

## Supplementary References

1.  Itu, L. *et al.* A machine-learning approach for computation of fractional flow reserve from coronary computed tomography. *J. Appl. Physiol.* **121**, 42–52 (2016).

2.  Lee, S. & You, D. Prediction of laminar vortex shedding over a cylinder using deep learning. *arXiv Prepr. arXiv1712.07854* (2017).

3.  Guo, X., Li, W. & Iorio, F. Convolutional neural networks for steady flow approximation. in *Proceedings of the 22nd ACM SIGKDD international conference on knowledge discovery and data mining* 481–490 (2016).

4.  Liang, L., Mao, W. & Sun, W. A feasibility study of deep learning for predicting hemodynamics of human thoracic aorta. *J. Biomech.* **99**, 109544 (2020).

5.  Taylor, C. A., Hughes, T. J. R. & Zarins, C. K. Finite element modeling of blood flow in arteries. *Comput. Methods Appl. Mech. Eng.* **158**, 155–196 (1998).

6.  Longest], P. [Worth & Kleinstreuer, C. Comparison of blood particle deposition models for non-parallel flow domains. *J. Biomech.* **36**, 421–430 (2003).

7.  Chiou, M. C. Particle deposition from natural convection boundary layer flow onto an isothermal vertical cylinder. *Acta Mech.* **129**, 163–176 (1998).

8.  Dyedov, V. *et al.* Variational Generation of Prismatic Boundary-Layer Meshes for Biomedical Computing. *Int. J. Numer. Methods Eng.* **79**, 907–945 (2009).

9.  Febina, J., Sikkandar, M. Y. & Sudharsan, N. M. Wall Shear Stress Estimation of Thoracic Aortic Aneurysm Using Computational Fluid Dynamics. *Comput. Math. Methods Med.* https://doi.org/10.1155/2018/7126532 (2018)

# Representative Publications 2:

## Pulse-Wave-Pattern Classification with a Convolutional Neural Network

**Gaoyang Li[1,2], Kazuhiro Watanabe[1,2], Hitomi Anzai[2], Xiaorui Song[3], Aike Qiao[4], Makoto Ohta[2,5*]**

[1]Institute of Fluid Science, Tohoku University, 2-1-1, Katahira, Aoba-ku, Sendai, Miyagi ,980-8577, Japan

[2] Graduate School of Biomedical Engineering, Tohoku University 6-6 Aramaki-aza-aoba, Aoba-ku Sendai Miyagi 980-8579, Japan

[3]Department of Radiology, Taishan Medical University, No.619 Greatwall Road, Daiyue District, Taian, Shandong, 271000, China

[4]College of Life Science and Bioengineering, Beijing University of Technology, No.100, Pingleyuan, Chaoyang District, Beijing, 100022, China

[5]ELyTMaX UMI 3757, CNRS–Université de Lyon–Tohoku University

[*]Corresponding author: makoto.ohta@tohoku.ac.jp

**Abstract**

Owing to the diversity of pulse-wave morphology, pulse-based diagnosis is difficult, especially pulse-wave-pattern classification (PWPC). A powerful method for PWPC is a convolutional neural network (CNN). It outperforms conventional methods in pattern classification due to extracting informative abstraction and features. For previous PWPC criteria, the relationship between pulse and disease types is not clear. In order to improve the clinical practicability, there is a need for a CNN model to find the one-to-one correspondence between pulse pattern and disease categories. In this study, five cardiovascular diseases (CVD) and complications were extracted from medical records as classification criteria to build pulse data set 1. Four physiological parameters closely related to the selected diseases were also extracted as classification criteria to build data set 2. An optimized CNN model with stronger feature extraction capability for pulse signals was proposed, which achieved PWPC with 95% accuracy in data set 1 and 89% accuracy in data set 2. It demonstrated that pulse waves are the result of multiple physiological parameters. There are limitations when using a single physiological parameter to characterise the overall pulse pattern. The proposed CNN model can achieve high accuracy of PWPC while using CVD and complication categories as classification criteria.

**Introduction**

Pulse waves contain a large quantity of pathological and physiological information[1,2]. Pulse-wave characteristics are closely related to diseases (hypertension, type 2 diabetes, atherosclerosis, etc.), especially cardiovascular diseases (CVD) and physiological parameters [pulse-wave velocity, cardio-ankle vascular index (CAVI), blood pressure, etc.][3,4]. Therefore, pulse analysis is extensive used in cardiovascular function assessment and non-invasive early diagnosis of cardiovascular disease and related complications[5]. TCPD (Traditional Chinese Pulse Diagnosis) refers to the diagnosis of diseases via traditional Chinese medical practices by feeling the change in pulse at the patient's wrist, which is highly dependent on the doctor's skill and experience[6]. Computer-aided analysis has made some achievements in pulse diagnosis, especially in pulse-wave-pattern classification (PWPC). For example, Wang et al. divided 407 sets of pulse data into five pulse patterns by using a Bayesian network based on six pulse parameters: depth, width, length, frequency, rhythm and strength (84% successful classification rate)[7]. Moreover, Xu et al. divided 320 sets of pulse data

into 16 pulse patterns by using a fuzzy neural network based on differences in pulse shapes, widths, positions and some specific local parameters (90% successful classification rate)[8]. However, the diverse morphology of pulse waves remains a difficulty for PWPC, which may lead to problems such as waveform local time shifting, as shown in Figure 1[9]. In addition, the classification criteria of these studies are based on TCPD theory, which means that a pulse pattern may correspond to a variety of disease categories, as shown in Figure 1[10]. It also leads to a decrease in the clinical practicality of pulse-based diagnosis. Thus, in this study, we selected new classification criteria—that is, the CVD and complication categories and the clinical physiological parameters—with the aim of developing a practical PWPC method with a high classification rate.
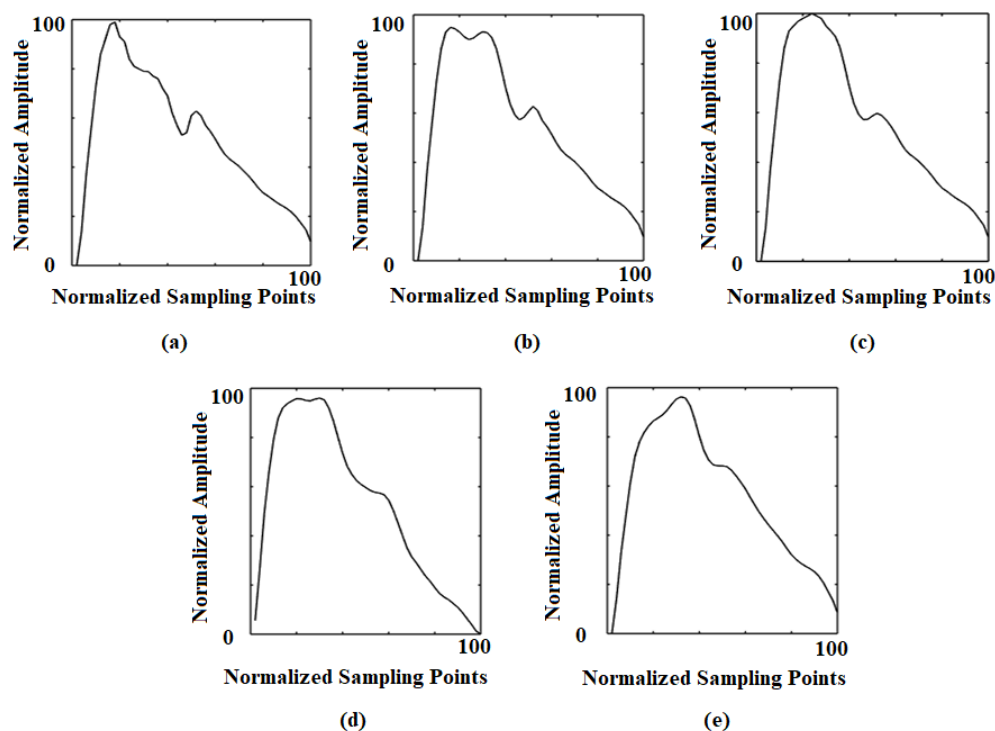


**Figure 1.** According to previous studies' classification criteria, we show five pulse waves that exhibit a taut pulse pattern, which involves a pulse with a high second peak (local time shifting), as follows: (a) typical taut pulse, (b) taut pulse with high tidal wave and (c) taut pulse with tidal wave merged with percussion wave.[9] With the help of medical doctors, (d) and (e) were extracted from our database. Although a–e all feature a taut pulse pattern, there are still differences in some local waveform characteristics. In addition, the subject of (d) suffered from hyperlipidaemia, while the subject of (e) suffered from atherosclerosis. This shows that, under the previous classification criteria, a single pulse pattern might correspond to many disease categories.

With the research and development of deep learning, various of neural network structures have been designed for signal processing. Recurrent neural network (RNN)[11], based on its internal memory, is used to process arbitrary time series input sequence such as non-segmented handwriting recognition, speech recognition, etc. Long short term memory (LSTM)[12], as a variant of RNN, can effectively prevent the occurrence of gradient vanishing from processing time series signals. In recent years, remarkable achievements have been made in the field of pattern classification via the use of convolutional neural networks (CNNs) as deep learning

structures[13,14,15,16]. CNNs provide an end-to-end learning model. The trained CNNs by the gradient descent method can learn the characteristics of input data and further complete the pattern classification. CNNs have strong ability of feature learning and pattern classification. The main reason is that the features of the lower layers are derived from the partial information and convolution kernel with sharing weights from the upper layer. CNNs have been applied in the classification of human physiological signal patterns. Based on a 34-layer CNN, Rajpurkar et al. classified the electrocardiogram (ECG) signals into 14 types[17]. Moreover, Rubin et al. performed heart-sound recordings based on deep CNN and Mel-frequency cepstral coefficients[18]. These studies used CNN to achieve pattern classification of relevant physiological signals and achieved higher accuracy than the diagnostic results of experienced physicians. Furthermore, Hu et al. used CNN to divide pulse waves into two types: health and subhealth[19]. In the present study, in view of the large amount of pathological and physiological information contained in pulse signals, we collected the required data under the guidance of the doctor and established two data sets based on either CVD/complication categories or physiological parameters. We proposed an optimised CNN model for PWPC based on these two data sets. The purpose of this study was to identify a practical and efficient classification criterion for PWPC based on CNN, which contributed to non-invasive, practical and effective diagnosis of CVDs and related complications.

**Results**

The average pulse waves of each pattern in the two data sets are shown in Figure 2.
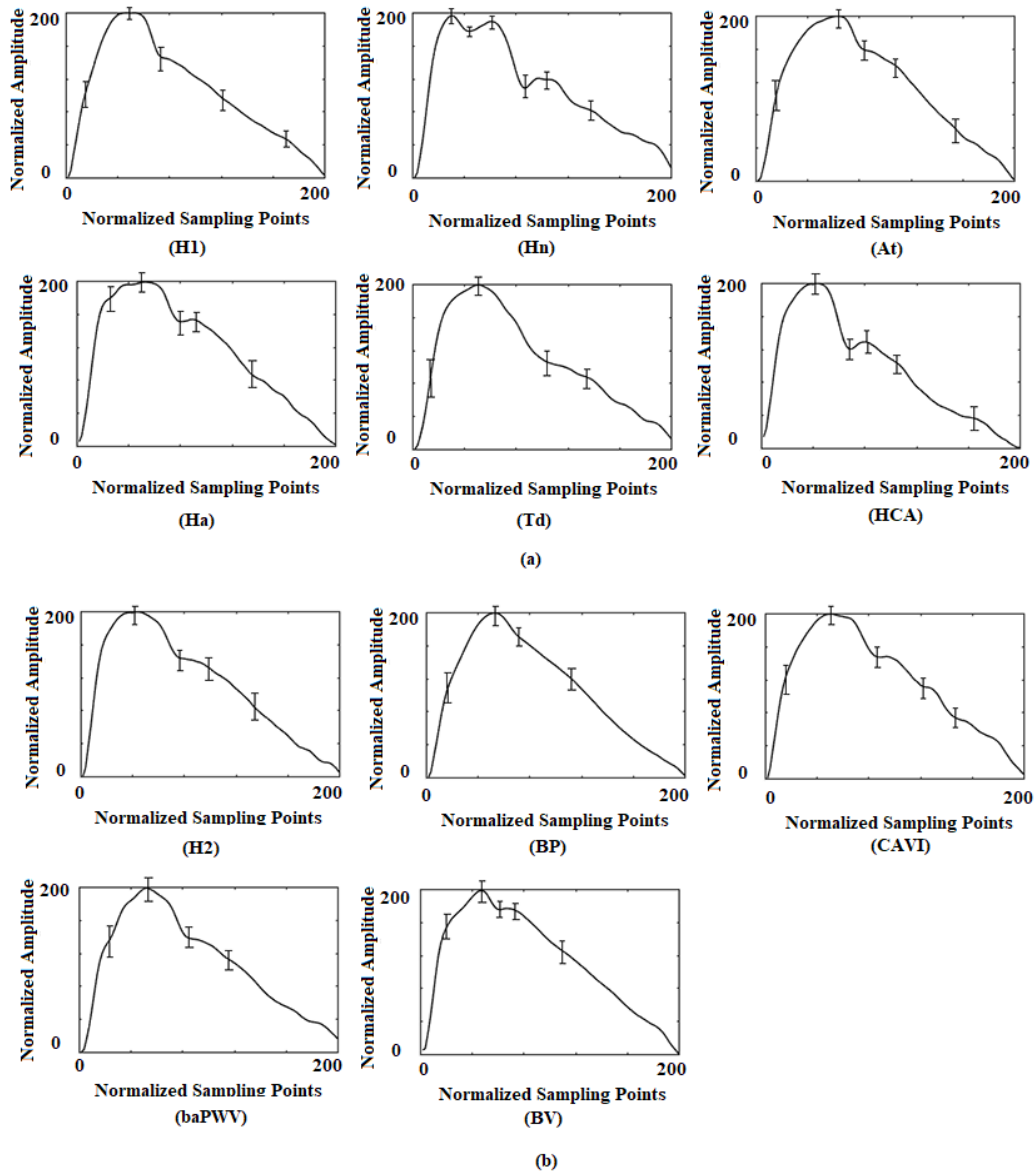
**Figure 2.** Average pulse-wave patterns in data set 1 (a) and data set 2 (b). Abbreviation Represents Pulse Wave Patterns: H1-Healthy Control Group in Data Set 1; Hn- hypertension; At-atherosclerosis; Ha-hyperlipidaemia; Td-type 2 diabetes; HCA-Hypertension complicated by atherosclerosis; H2-Healthy Control Group in Data Set 2; BP-blood pressure; baPWV- brachial-ankle pulse wave velocity; BV-blood viscosity.

We showed the learning curves of data set 1 and data set 2 respectively to evaluate their PWPC performance on the proposed CNN model, as shown in Figure 3. For cost-value curve, the decline rate of data set 1 was significantly higher than that of data set 2. For training error and test error, the minimum value of data set 1 was smaller than that of data set 2. Especially test error, data set 1 (When epoch was 90, the minimum test error was 0.08. Epoch was the number of iterations in CNN pattern classification) was much smaller than data set 2 (When epoch was 100, the minimum test error was 0.34). With the same proposed CNN, the six pulse

patterns in data set 1 showed higher calculation efficiency and feature expression ability than those five patterns in data set 2.
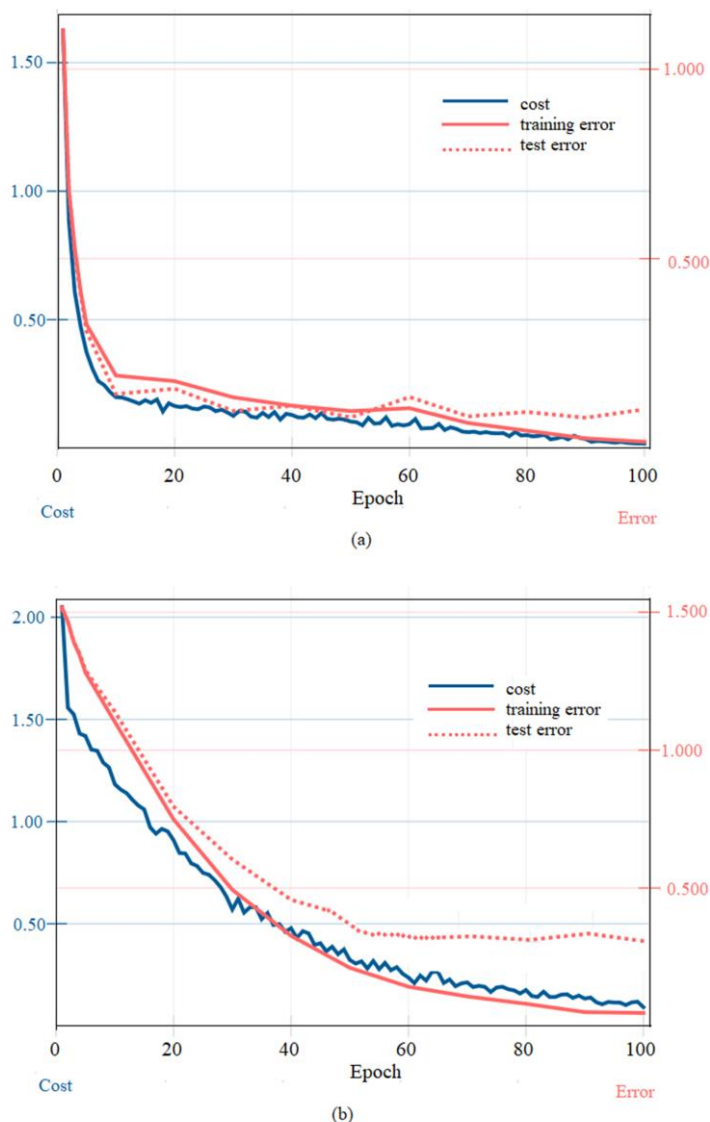


**Figure 3.** Learning curve in data set 1 (a) and data set 2 (b).

Table 1 shows the overall values of the evaluation parameters in the two data sets. The accuracy and other evaluation parameters of PWPC in data set 1 (overall accuracy = 0.95) were higher than those in data set 2 (overall accuracy = 0.89). Tables 2 and 3 show the details for each pattern in the two data sets separately. Pulse-wave patterns representing healthy subjects (H1 and H2) could be identified with high precision (precision H1 = 1, recall H1 = 0.99; precision H2 = 0.97, recall H2 = 0.97). The HCA, as the pulse pattern of complications, had the lowest classification rate in data set 1 (precision HCA = 0.89, recall HCA = 0.91). In addition, the classification performance of other pulse patterns in data set 1 was higher than that in data set 2.

**Table 1.** PWPC evaluation of per pulse patterns in two data sets

| Data set | Overall accuracy | Overall precision | Overall recall | Overall F-measure |
|---|---|---|---|---|
| Data set 1 | 0.95 | 0.95 | 0.95 | 0.95 |
| Data set 2 | 0.89 | 0.89 | 0.89 | 0.89 |

**Table 2.** PWPC evaluation of per pulse patterns in data set 1

| Pulse pattern | Precision | Recall | F-measure |
|---|---|---|---|
| H1 | 1 | 0.99 | 0.99 |
| Hn | 0.94 | 0.93 | 0.94 |
| At | 0.90 | 0.94 | 0.92 |
| Ha | 1 | 0.99 | 0.99 |
| Td | 0.96 | 0.93 | 0.94 |
| HCA | 0.89 | 0.91 | 0.90 |

**Table 3.** PWPC evaluation of per pulse patterns in data set 2

| Pulse pattern | Precision | Recall | F-measure |
|---|---|---|---|
| H2 | 0.97 | 0.97 | 0.97 |
| BP | 0.89 | 0.89 | 0.89 |
| CAVI | 0.82 | 0.84 | 0.83 |
| baPWV | 0.84 | 0.87 | 0.85 |
| BV | 0.95 | 0.89 | 0.92 |

To further assess the PWPC result of the proposed CNN model, the two data sets were put into different neural networks models for PWPC. Table 4 shows the accuracy of PWPC with those different models. It details network methods, classification criteria, number of subjects, and the accuracy. It demonstrated that compared with other neural networks or other CNN structures, our proposed CNN model achieved higher accuracy in PWPC under the new classification criteria, which also meant stronger feature extraction ability for pulse signals.

**Table 4.** PWPC accuracy of different methods

| Network | Method | Classification criteria | Number of subjects | Accuracy |
|---|---|---|---|---|
| The proposed | CNN | CVD and complications | 412 | **0.95** |
| CNN model | CNN | Physiological parameters | 412 | 0.89 |
| LetNet[20] | CNN | CVD and complications | 412 | 0.69 |
| | CNN | Physiological parameters | 412 | 0.63 |
| AlexNet[14] | CNN | CVD and complications | 412 | 0.73 |
| | CNN | Physiological parameters | 412 | 0.70 |
| VGG-Net[15] | CNN | CVD and complications | 412 | 0.81 |
| | CNN | Physiological parameters | 412 | 0.79 |
| Wang's network[7] | Bayesian Network | Based on TCPD | 407 | 0.84 |
| Xu's network[8] | Fuzzy Neural Network | Based on TCPD | 320 | 0.90 |

To further analyse the causes of errors in pattern classification, we determined the confusion matrix of the two data sets, as shown in Figure 4. The cause of errors in data set 1 was mainly the erroneous classification of the four pulse patterns of Hn, At, HCA and Td. In data set 2, with the exception of the control group (H2), the remaining four pulse patterns (BP, CAVI, baPWV and BV) were found to interfere with each other and have higher error rates.
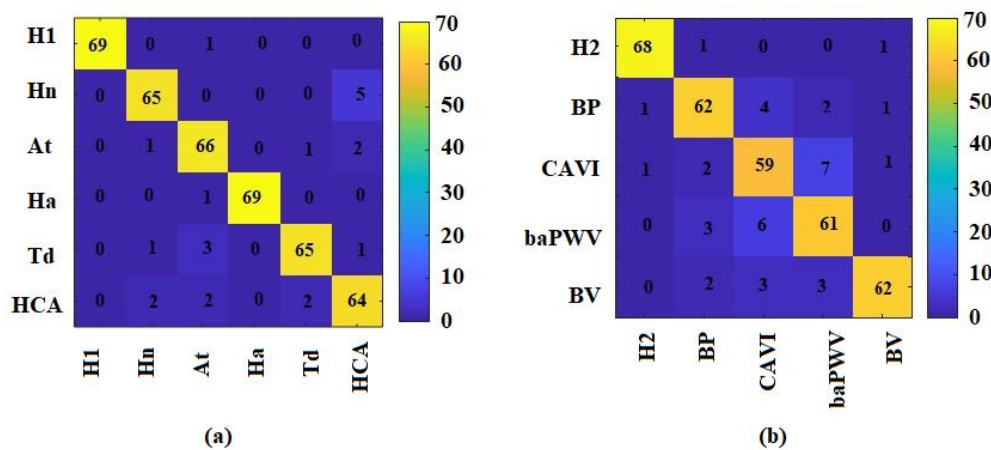


**Figure 4.** The confusion matrices of data set 1 (a) and data set 2 (b). The confusion matrix is an intuitive method for evaluating the results of pattern classification CNN models. The real categories (rows) and predicted categories (columns) of the classification results can be read directly. For example, in matrix (a),

there were 70 (65 + 5) pulse waves which really belonged to the Hn pattern (the second row), while the CNN model predicted 69 (65 + 1 + 1 + 2) pulse waves in the Hn pattern (the second column).

**Discussion**

In this study, CVD and associated complications as well as related physiological parameters were extracted, which were used as classification criteria. According to the new classification criteria, we screened the subjects' pulse waves and created data set 1 and data set 2, respectively. An optimised CNN model was proposed for PWPC. It achieved the classification of six pulse patterns in data set 1 with an accuracy of 95% and the classification of six pulse patterns in data set 2 with an accuracy of 89%. The main contributions of this study are as follows:

1. Two pulse wave data sets were created, which contained a large amount of physiological and pathological information of subjects.

2. New classification criteria and optimized CNN model were proposed, which achieves higher accuracy than previous studies[7,8,19,21,22].

This study demonstrates that CVD and complications are practical and efficient classification criteria, enabling the optimised CNN model to achieve high accuracy for PWPC.

We observed that the classification errors in data set 1 were mainly due to the erroneous classification of the Hn, At and HCA patterns. This was due to the simultaneous occurrence of hypertension and atherosclerosis on behalf of HCA. There must be some similar pulse characteristics between HCA and the other two diseases, which indicates that, in order to ensure that the characteristics of the different pulse patterns are typical, the selected data specimen must exclude the effect of complications at the same time. In addition, in data set 1, Td was also partially misclassified as Hn (n = 1), At (n = 3) and HCA (n = 1). Previous studies showed that type 2 diabetes could increase the risk and mortality of CVD, and they had similarities in the damage to the cardiovascular system[23,24,25]. Thus, there might have been similar pulse waveform characteristics between Td and Hn, At, HCA patterns, which led to classification errors.

In data set 2, four pulse patterns (BP, CAVI, baPWV and BV) were found to interfere with each other in pattern classification. Previous studies showed that the effect of a single physiological parameter on pulse waveform was mainly reflected in the change of some local characteristics[26,27,28]. The pulse waveform characteristics with the same value of one specific physiological parameter would change as a result of the differences of other physiological parameters, as shown in Figure 5. It may have led to the errors of pattern classification in data set 2. Our study showed that the pulse-wave was the result of multiple physiological parameters. There are clearly limitations associated with using a single physiological parameter in

characterising the overall pulse pattern. Disease was the result of multiple physiological parameters, which might explain the higher classification accuracy in data set 1.
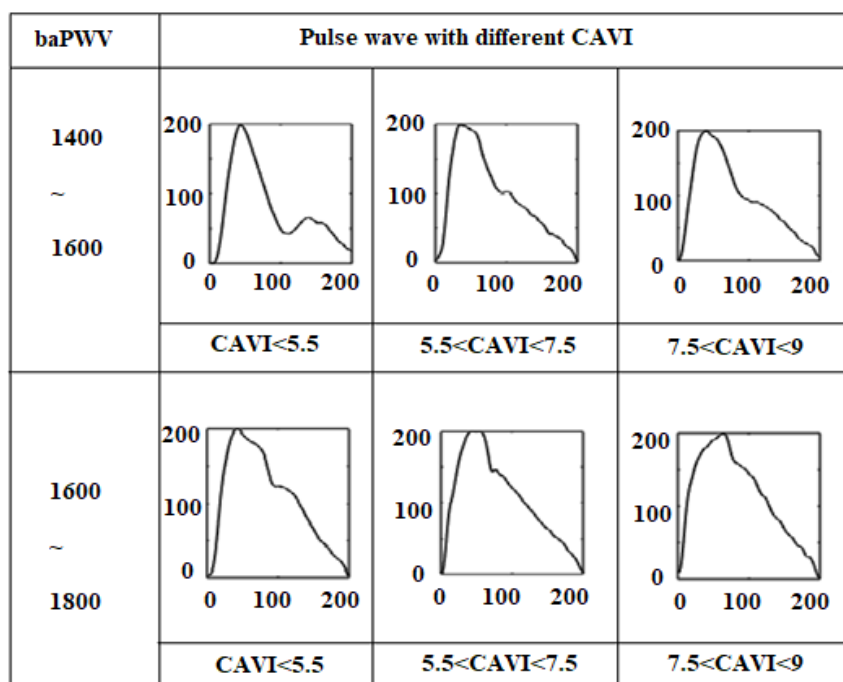


**Figure 5.** The pulse-wave form baPWV pulse pattern with the different baPWV and different CAVI. Pulse waves from six subjects were selected.

This study had several limitations. The most important one was the relatively limited number of subjects. Limited by the number of subjects, the effects of some physiological information such as age, height and weight on pulse waveform were ignored, which inevitably led to errors in pattern classification[1]. However, in our study, the number of pulse waves in each pulse pattern was several times that in some previous studies[22,29]. To some extent, the findings indicated that each of our patterns could represent the typical pulse characteristics. In addition, this study focused on the classification criteria of pulse patterns. For this purpose, we used the same CNN model to classify two data sets. Regarding the low classification rate of data set 2, we did not explore whether it could be improved by optimising the architecture of the CNN model.

**Conclusions**

In this study, we established pulse wave data set 1 and data set 2 based on the classification criteria: CVD categories and related physiological parameters. CNN was used to extract features from two data sets and to achieve PWPC with high accuracy. The main contribution of this study is to propose the new classification criteria for PWPC and construct a matching CNN model. The optimized CNN model achieved PWPC with 95% accuracy in data set 1 and 89% accuracy in data set 2. This study demonstrated that pulse waves are the result of multiple physiological parameters, so there are limitations when using a single physiological

parameter to characterize the overall pulse pattern. The proposed CNN model can achieve high accuracy PWPC while using CVD and complication categories as classification criteria, which contributes to non-invasive, practical and effective diagnosis of CVD and associated complications.

## Method

### Data collection

The original pulse wave data were from the "Study on Evaluation Method of Cardiovascular System Based on Non-invasive Detection of Blood Pressure and Pulse-Wave of Limbs[30]", which recruited 412 subjects and determined their physiological parameters and more than 12,000 cycles of pulse waves. The pulse and blood pressure signal measuring device was Fukuda VS-1500A. In addition, the subjects' brachial ankle pulse-wave velocity (baPWV) and blood viscosity were collected. All subjects were registered at Beijing University of Technology Hospital, and information on their diseases was collected through the subjects' medical records.

The study with its experimental protocols and relevant details was approved by the Institutional Ethics Committee of Beijing University of Technology and Tohoku University. All experiments were performed in accordance with relevant guidelines and regulations. We explained the content of the study to the subjects in detail, and on this basis, the subjects signed the informed consent form.

### Pulse waveform denoising and normalisation

In this study, we collected the pulse signals from the wrist of the subjects. The denoising and normalization of pulse signals were processed with the same method as the previous studies[31]. Firstly, the noise was removed with wavelet transform decomposition method[32]. Then, in order to prevent the distortion of pulse signals, according to Nyquist theorem and actual sampling frequency[8,19], the sampling points of single cycle of pulse wave were set at 200. Because the focus of this study was the change of pulse wave model, the amplitude of pulse wave was normalized to 0-200 in each cycle.
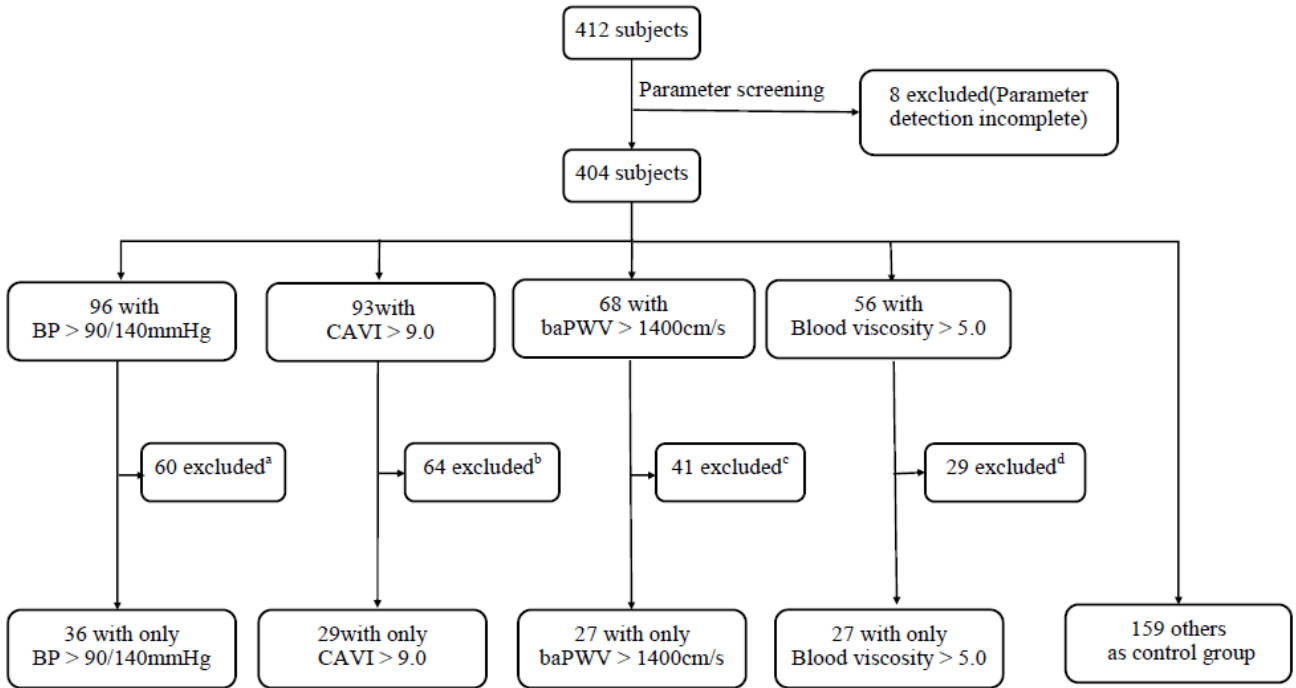
### Data sets

Previous studies classified pulses into patterns based on the TCPD theory[7,8,9,10,33]. However, as mentioned previously, under this classification criterion, one pulse pattern may correspond to a variety of disease categories. Thus, in this study, based on subjects' clinical data, we directly selected five diseases as new classification criteria: hypertension, atherosclerosis, hyperlipidaemia, type 2 diabetes and hypertension complicated by atherosclerosis (HCA). Type 2 diabetes, as one of the common complications of CVD[34], and HCA were used to study the effects of CVD complications on pulse waves. To ensure the typical characteristics of each pulse pattern, the pulse signals from subjects who only suffered from one of the five diseases and healthy subjects (a total of six types) were used as new pulse patterns to build data set 1, as shown in Figure 6.
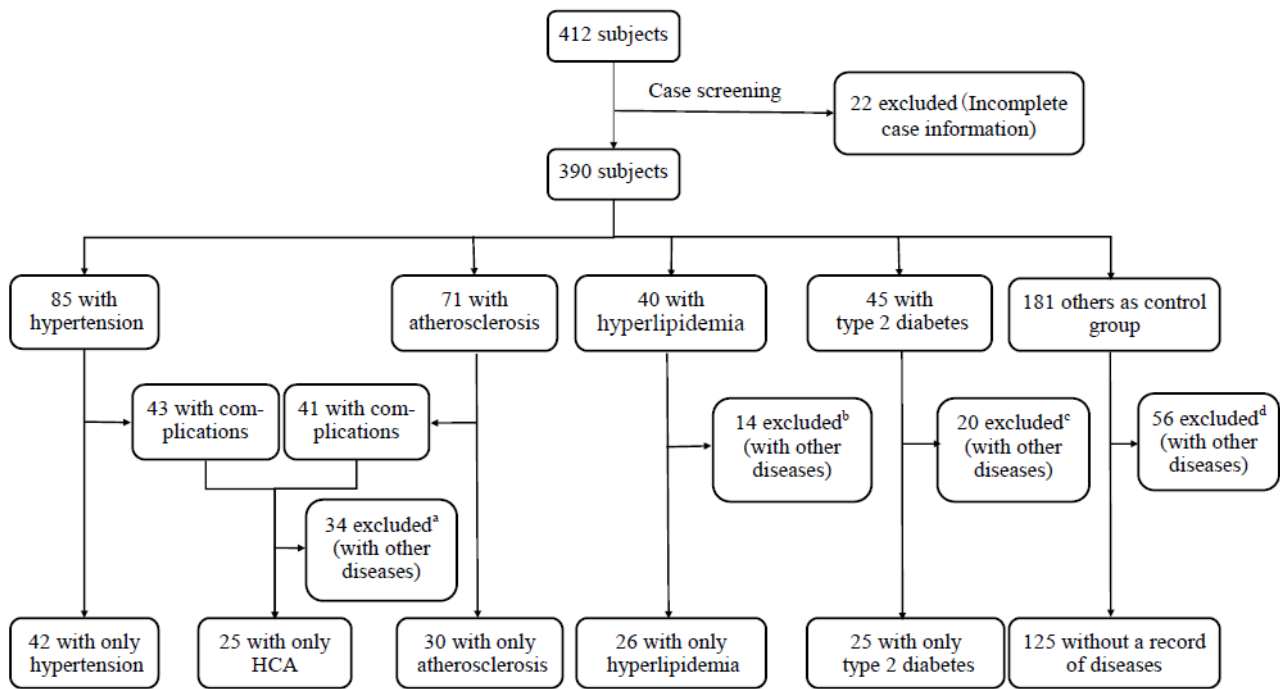
**Figure 6.** The process of screening the subjects in data set 1.[a,b,c,d] Screening criteria: The number of subjects for a selected disease should be more than 20. The disease or complications must be of the five types selected in this study. There is no serious abnormality in pulse waves caused by noise or incorrect data collection, among others. We show all cases and numbers of excluded subjects in [c]: type 2 diabetes complicated by hypertension (n = 4), type 2 diabetes complicated by atherosclerosis (n = 3), type 2 diabetes complicated by heart failure (n = 5) and diabetic foot disease (n = 8). Based on the screening criteria, we excluded these cases.

We simultaneously selected four physiological parameters closely related to the selected diseases as classification criteria: blood pressure, which can be used as an indicator for assessing hypertension[35]; cardio-ankle vascular index (CAVI), which is one of the indicators for assessing atherosclerosis[36]; and brachial ankle pulse-wave velocity (baPWV), which can be used as an indicator for evaluating cardiovascular function in type 2 diabetics[37]; For patients with hyperlipidaemia, an increase of blood lipids often occurs simultaneously with increased blood viscosity[38]. Based on the subjects in data set 2 and the medical reference range, we determined the range of each physiological parameter. The pulse waves of subjects in whom only one of the four parameters was beyond the range were selected. The pulse waves of subjects whose four parameters were all within the range were also selected as a healthy control group. Then the five types of pulse pattern were used to build data set 2, as shown in Figure 7.

**Figure 7.** The screening process of the subjects in data set 2.[a,b,c,d] Screening criteria: The number of subjects for selected parameters should be more than 20. Subjects' other parameters, such as stroke output and cardiac output, must be within the normal range of medical reference. There is no serious abnormality in pulse-wave caused by noise or incorrect data collection, among others. For [a,b,c,d], most of the excluded subjects had three or even four parameter values outside of the range. To ensure that the characteristics of each pulse pattern were typical, we excluded these subjects.

For the processing of pulse image, this study used the same method as previous studies[31]. We extracted the pulse cycles from the selected subjects. To avoid data duplication affecting the accuracy of CNN prediction, all pulse waves in the two data sets were taken from different cycles. The total cycles of each pulse pattern were 210, which were divided into training set and test set, as shown in Table 5. As mentioned above, the number of sampling points in a single cycle of normalized pulse wave was 200, and the amplitude was 0-200. Therefore, the pulse wave signals were processed as input PNG pulse images with a size of 200 x 200 pixels.

**Table 5.** The details of PWPC data sets.

| | Pulse categories | Total pulse number | Training number | Test number | Type of disease or physiological parameters (range) |
|---|---|---|---|---|---|
| Data set 1 | H1 | 210 | 140 | 70 | Healthy control group in data set 1 |
| | Hn | 210 | 140 | 70 | Only hypertension |
| | At | 210 | 140 | 70 | Only atherosclerosis |
| | Ha | 210 | 140 | 70 | Only hyperlipidaemia |
| | Td | 210 | 140 | 70 | Only type 2 diabetes |
| | HCA | 210 | 140 | 70 | Hypertension complicated by atherosclerosis |
| Data set 2 | H2 | 210 | 140 | 70 | Healthy control group in data set 2 |
| | BP | 210 | 140 | 70 | Only high blood pressure (>90/140 mmHg) |
| | CAVI | 210 | 140 | 70 | Only CAVI (>9.0) |
| | baPWV | 210 | 140 | 70 | Only baPWV (>1400 cm/s) |
| | BV | 210 | 140 | 70 | Only blood viscosity (>5.0) |

**The proposed CNN**

In this study, an optimised CNN model (10-layer) was proposed based on DCNN[19] and LeNet-5[20], which had been applied for PWPC, as shown in Figure 8. Compared with the previous networks, we added dropout[39] between the third max pooling layer and the fully connected layer. When CVDs were used as classification criteria, each pulse pattern changed from local waveform difference under previous criteria to overall pulse waveform difference. This led to too many characteristic parameters of pulse wave extracted by CNN, which further led to over-fitting in the training process. Pre-experimental results showed that dropout layer could help reduce test errors and avoid over-fitting phenomenon in the training process (see Supplementary Fig. S1 online). In addition, the final Softmax activation produced a distribution over the output probability classes for each pulse pattern of two data sets. Besides the layers mentioned above, the CNN also included three convolution layers, three max pooling layers and two fully connected layers. The number of convolution layers was determined by the number of pulse wave characteristic. The insufficient layers led to the inadequate feature extraction ability of CNN, while the excessive layers increased the time cost and calculation cost. In this study, we determined the number of layers by pre-experimental results. The convolutional layers were used to extract complex parameters of the input feature maps by convolution with kernels. The max pooling layers achieved the down-sampling of the input signals by choosing the maximum value of the area as the value of the pooled area. The max pooling layers could retain the main features of the input signals while reducing the parameters and computation, which helped to avoid the occurrence of over-fitting and improve the generalization ability of the CNN model[40]. The final two fully connected layers

combined all of the upper feature maps into a one-dimensional array, which was used to classify the output. In this study, we used the Adam optimiser, which is straightforward to implement, with high calculation efficiency and low memory requirements[41]. In accordance with previous studies and a preliminary experiment, the parameters of the Adam optimiser were as follows: learning rate = 0.001, $\epsilon = 0.001$, $\rho 1 = 0.9$, $\rho 2 = 0.999$ and $\delta = 1E^{-8}$. During the optimisation process, we saved the best model configuration as evaluated on the test set. The CNN was trained by neural_network_console (Sony Company) on an Intel(R) HD Graphics 630 with batch size 64 for 100 epochs.
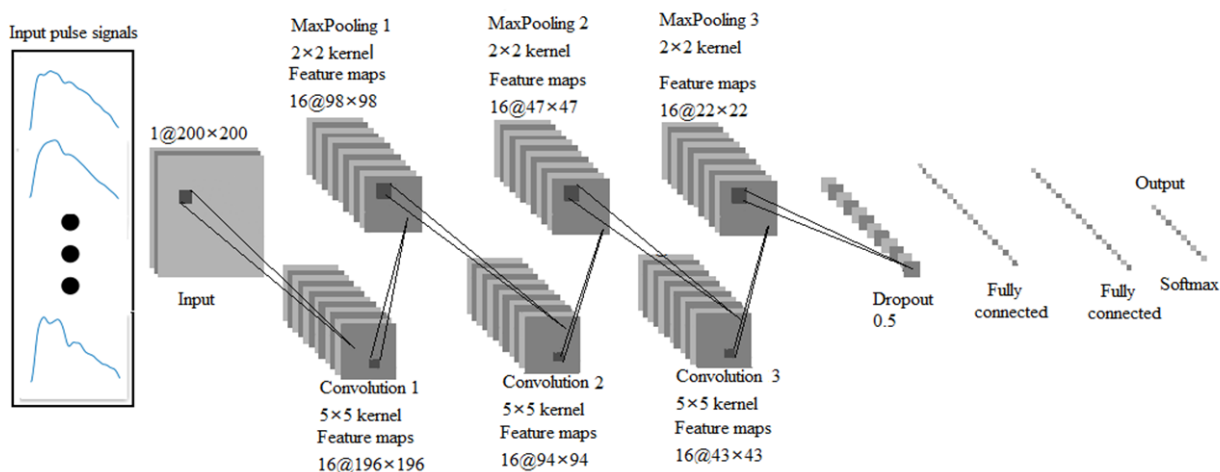


**Figure 8.** An illustration of the CNN architecture. The size settings of convolution kernels and feature maps are shown in the figure.

**Evaluation**

The proposed CNN was evaluated with the average of the operating parameters calculated over time. The overall accuracy, precision, recall and F-measure were determined to assess the classification performance of the network, as presented in the results section. To further evaluate the classification performance of each pulse pattern, we also present the evaluation parameters of each pattern and the confusion matrices for the two test sets. The evaluation parameters were calculated using the true positive (TP), true negative (TN), false positive (FP) and false negative (FN).

In order to further evaluate the PWPC capability of the CNN model proposed in this study, we selected three different neural networks (LetNet[20], AlexNet[14], VGG-Net[15]). Data set 1 and data set 2 were used as inputs of these three networks respectively. The PWPC results were compared with the CNN model proposed in this study.

**Acknowledgement**

**Author Contributions**

**Additional Information**

**Competing Interests:** The authors declare no competing interests.

**Data Availability**

The datasets analysed during the current study are available from the corresponding author on reasonable request.

**References**

1.  O'Rourke, M. F., Pauca, A. & Jiang, X.-J. Pulse wave analysis. *Br. J. Clin. Pharmacol.* **51,** 507–522 (2001).

2.  Korpas, D., Hálek, J. & Doležal, L. Parameters describing the pulse wave. *Physiol. Res.* **58,** 473–479 (2009).

3.  Safar, M. E., Levy, B. I. & Struijker-Boudier, H. Current perspectives on arterial stiffness and pulse pressure in hypertension and cardiovascular diseases. *Circulation* **107,** 2864–2869 (2003).

4.  Yamashina, a *et al.* Brachial-ankle pulse wave velocity as a marker of atherosclerotic vascular damage and cardiovascular risk. *Hypertens. Res.* **26,** 615–622 (2003).

5.  Cohn, J. N. *et al.* Noninvasive pulse wave analysis for the early detection of vascular disease. *Hypertension* **26,** 503–508 (1995).

6.  Shu, J. J. & Sun, Y. Developing classification indices for Chinese pulse diagnosis. *Complement. Ther. Med.* **15,** 190–198 (2007).

7.  Wang, H. & Cheng. A quantitative system for pulse diagnosis in Traditional Chinese Medicine. *Conf. Proc. IEEE Eng. Med. Biol. Soc.* **6,** 5676-5679 (2005).

8.  Xu, L., Meng, Q. H., Wang, K., Lu, W. & Li, N. Pulse images recognition using fuzzy neural network. *Expert Syst. Appl.* **36,** 3805–3811 (2009).

9.  Zuo, W., Zhang, D., Zhang, D., Zhang, H. & Li, N. Classification of pulse waveforms using edit distance with real penalty. *EURASIP J. Adv. Signal Process.* **2010,** (2010).

10. Xu, L. S., Wang, K. Q. & Wang, L. Pulse Waveforms Classification Based on Wavelet Network. *IEEE EMBS.* 4596–4599 (2005).

11. Graves, A., Mohamed, A. & Hinton, G. Speech recognition with deep recurrent neural networks. *2013 IEEE International Conference on Acoustics, Speech and Signal Processing* 6645–6649 (2013)

12. Greff, K., Srivastava, R. K., Koutnik, J., Steunebrink, B. R. & Schmidhuber, J. LSTM: A Search Space Odyssey. *IEEE Trans. Neural Networks Learn. Syst.* **28,** 2222–2232 (2017).

13. Huang, G. B., Lee, H. & Learned-Miller, E. B. T.-I. C. on C. V. and P. R. Learning hierarchical representations for face verification with convolutional deep belief networks. in 2518–2525 (2012).

14. Krizhevsky, A., Sutskever, I. & Hinton, G. E. B. T.-I. C. on N. I. P. S. ImageNet classification with deep convolutional neural networks. *NIPS.* 1097–1105 (2012).

15. Simonyan, K. & Zisserman, A. Very Deep Convolutional Networks for Large-Scale Image

Recognition. *Comput. Sci.* (2014).

16. zhang, J., liu, P., Zhang, F. & Song, Q. CloudNet: Ground-based Cloud Classification with Deep Convolutional Neural Network. *Geophys. Res. Lett.* 1–8 (2018). doi:10.1029/2018GL077787

17. Rajpurkar, P., Hannun, A. Y., Haghpanahi, M., Bourn, C. & Ng, A. Y. Cardiologist-Level Arrhythmia Detection with Convolutional Neural Networks. (2017).

18. Rubin, J. *et al.* Classifying heart sound recordings using deep convolutional neural networks and mel-frequency cepstral coefficients. *Computing in cardiology conference (CinC)*. 813-816 (2016).

19. Hu, X., Zhu, H., Xu, J., Xu, D. & Dong. Wrist pulse signals analysis based on Deep Convolutional Neural Networks. *2014 IEEE Conference on, J. B. T.-C. I. in B. and C. B*. in 1–7 (2014).

20. Lécun, Y., Bottou, L., Bengio, Y. & Haffner, P. Gradient-based learning applied to document recognition. *Proc. IEEE* **86,** 2278–2324 (1998).

21. Bo, I. *et al.* Cardiovascular Morbidity and Mortality Associated With the Metabolic Syndrome. *Diabetes Care* **24,** 683-689 (2001).

22. Yang, W., Zhang, L. & Zhang, D. Wrist-Pulse Signal Diagnosis Using ICPulse. *Proceedings of the 27th Annual International Conference of the Engineering in Medicine and Biology Society (EMBS '05)*. 5676–5679, (2009).

23. Kannel, W. B. & Mcgee, D. L. Diabetes and Cardiovascular Disease: The Framingham Study. *Am. J. Cardiol.* **35,** 2035–2038 (1979).

24. Grøntved, A. & Hu, F. B. Television Viewing and Risk of Type 2 Diabetes, Cardiovascular Disease, and All-Cause Mortality A Meta-analysis. *Jama* **305,** 2448–2455 (2011).

25. Wilmot, E. G. *et al.* Sedentary time in adults and the association with diabetes, cardiovascular disease and death: systematic review and meta-analysis. *Diabetologia* **55,** 2895–2905 (2012).

26. Weber, T. *et al.* Wave reflections, assessed with a novel method for pulse wave separation, are associated with end-organ damage and clinical outcomes. *Hypertension* **60,** 534–541 (2012).

27. Hirata, K., Kawakami, M. & O'Rourke, M. F. Pulse Wave Analysis and Pulse Wave Velocity. *Circ. J.* **70,** 1231–1239 (2006).

28. Wang, A. *et al.* Quantification of radial arterial pulse characteristics change during exercise and recovery: *J. Physiol. Sci.* **68,** 1–8 (2018).

29. Zhang, S. R. & Sun Consumer and Control, Q. F. B. T.-I. S. on C. Human Pulse Recognition Based on Convolutional Neural Networks. in 366–369 (2016).

30. Song, X., Li, G., Qiao, A. & Chen, Z. Association of simultaneously measured four-limb blood pressures with cardiovascular function: a cross-sectional study. *Biomed. Eng. Online* **15,** 247–260 (2016).

31. Li, G., Anzai, H., Watanabe, K., Qiao, A. & Ohta, M. Pulse pattern classification of atherosclerotic patients based on convolutional neural network. *The Proceedings of the JSME Conference on Frontiers in Bioengineering* **2018.29,** 2C11 (2018).

32. Chang, F., Hong, W., Zhang, T., Jing, J. & Liu, X. Research on Wavelet Denoising for Pulse Signal Based on Improved Wavelet Thresholding. in *2010 First International Conference on Pervasive Computing, Signal Processing and Applications* 564–567 (2010). doi:10.1109/PCSPA.2010.142

33. Xu, L. *et al.* Objectifying Researches on Traditional Chinese Pulse Diagnosis. *Informatica Medica Slovenica.* **2,** 56-63 (2003).

34. Gæde, P. *et al.* Multifactorial Intervention and Cardiovascular Disease in Patients with Type 2 Diabetes. *N. Engl. J. Med.* **348,** 383–393 (2003).

35. Pessina, A. C. *et al.* Evaluation of hypertension and related target organ damage by average day-time blood pressure. *Clin. Exp. Hypertens.* **7,** 267 (1985).

36. Okura, T. *et al.* Relationship between Cardio-Ankle Vascular Index (CAVI) and Carotid Atherosclerosis in Patients with Essential Hypertension. *Hypertens. Res.* **30,** 335–340 (2007).

37. Arnett, D. K., Evans, G. W. & Riley, W. A. Arterial Stiffness: A New Cardiovascular Risk Factor? *Am. J. Epidemiol.* **140,** 669–682 (1994).

38. Irace, C. *et al.* Influence of blood lipids on plasma and blood viscosity. *Clin. Hemorheol. Microcirc.* **57,** 267–274 (2013).

39. Srivastava, N., Hinton, G., Krizhevsky, A., Sutskever, I. & Salakhutdinov, R. Dropout: a simple way to prevent neural networks from overfitting. *J. Mach. Learn. Res.* **15,** 1929–1958 (2014).

40. Microbiana, B. *et al.* Lung Pattern Classification for Interstitial Lung Diseases Using a Deep Convolutional Neural Network. *IEEE Trans. Med. Imaging* **35,** 1207–1216 (2016).

41. Kingma, D. P. & Ba, J. Adam: A Method for Stochastic Optimization. *Comput. Sci.* (2014). doi:10.1063/1.4902458

## Representative Publications 3:

# Research on Arterial Stiffness Status in Type 2 Diabetic Patients Based on Pulse Waveform Characteristics

**Gaoyang Li[1], Xiaorui Song[2], Aike Qiao[3], Makoto Ohta[4,5] [*]**

**Abstract:** For patients with type 2 diabetes, the evaluation of pulse waveform characteristics is helpful to understand changes in arterial stiffness. However, there is a lack of comprehensive analysis of pulse waveform parameters. Here, we aimed to investigate the changes in pulse waveform characteristics in patients with type 2 diabetes due to increased arterial stiffness.

In this study, 25 patients with type 2 diabetes and 50 healthy subjects were selected based on their clinical history. Age, height, weight, blood pressure, and pulse pressure were collected as the subjects' basic characteristics. The brachial-ankle pulse wave velocity (baPWV) was collected as an index of arterial stiffness. Parameters of time [the pulse wave period (T), the relative positions of peak point ($T_1$) and notch point ($T_2$), and pulse wave time difference between upper and lower limbs ($T_3$)] and area [the total waveform area (A), and the areas of the waveform before ($A_1$) and after ($A_2$) the notch point] were extracted from the pulse wave signals as pulse waveform characteristics. An independent sample t-test was performed to determine whether there were significant differences between groups. Pearson's correlation analysis was performed to determine the correlations between pulse waveform parameters and baPWV.

There were significant differences in $T_3$, A, $A_1$, and $A_2$ between the groups ($P < 0.05$). For patients with type 2 diabetes, there were statistically significant correlations between baPWV and $T_3$, A, $A_1$, and $A_2$ ($P < 0.05$).

This study quantitatively assessed changes in arterial pulse waveform parameters in patients with type 2 diabetes. It was demonstrated that pulse waveform characteristics ($T_3$, A, $A_1$, and $A_2$) could be used as indices of arterial stiffness in patients with type 2 diabetes.

**Keywords:** type 2 diabetes, pulse waveform, arterial stiffness

## 1. Introduction

Vascular endothelial dysfunction in patients with type 2 diabetes can affect the physiological structure of large and medium-sized arteries and microvascular structures, which can result in decreased vascular elasticity and abnormal structures of organs or tissues and may even lead to arteriosclerosis. A key aspect for type 2 diabetes treatment is early detection and application of suitable remedial measures to prevent the process of

---

[1]Graduate School of Biomedical Engineering, Tohoku University, Sendai, Miyagi, Japan.

[2]Department of Radiology, Taishan Medical University, No. 619 Greatwall Road, Daiyue District,Taian, Shandong, 271000, China.

[3]College of Life Science and Bioengineering, Beijing University of Technology, No.100, Pingleyuan, Chaoyang District, Beijing, 100022, CHINA.

[4]Institute of Fluid Science, Tohoku University, Sendai, 980-8577, Miyagi, Japan.

[5]ELyTMaX UMI 3757, CNRS – Université de Lyon – Tohoku University

[*] Corresponding Author: Makoto Ohta. Email: ohta@biofluid.ifs.tohoku.ac.jp

arteriosclerosis [Rydén, Standl, Bartnik et al. (2007)]. Therefore, the early detection of arterial stiffness is of great significance in clinical patients with type 2 diabetes.

Previous studies have shown that pulse wave velocity (PWV) can reflect arterial stiffness and can be used as a parameter for the early detection of arteriosclerosis in type 2 diabetes [Woolam, Schnur, Vallbona et al. (1962)]. The brachial-ankle PWV (baPWV), which is used as a risk indicator for diabetic complications is directly related to the incidence of type 2 diabetes [Aso, Miyata, Kubo et al. (2003)]. A high baPWV value can serve as an independent predictor of diabetic mortality and cardiovascular morbidity [Maeda, Inoguchi, Etoh et al. (2014)]. For patients with type 2 diabetes, parameters such as the Cardio-ankle vascular index (CAVI) calculated by PWV can also be used as indices of arteriosclerosis [Ibata, Sasaki, Kakimoto et al. (2008); Shirai, Hiruta, Song et al. (2011)]. However, owing to technical limitations, errors in PWV measurement inevitably arise [Hughes, Dixon and Mcveigh (2004)], and in most studies, only the pulse wave velocity was selected as the research object, ignoring the pulse waveform.

Noninvasive technology for detecting hemodynamics, represented by pulse wave detection and analysis, has been widely used as an important method of noninvasive detection of cardiovascular function because of its convenient and rapid measurement with high reliability [Allen (2007)]. Pulse waveform characteristics such as shape, amplitude, and period are closely related to the functional status of blood vessels. Pulse waves propagate in the arterial vessels and are constantly reflected at the downstream branches of all levels, thus, the pulse waves are not only affected by the heart but also by all levels of arteries and branches via a variety of physiological and pathological factors such as vascular resistance and arterial stiffness [Weber, Wassertheurer, Rammer et al. (2012); Hasegawa, Sato, Numano et al. (2011); Westerhof, Guelen, Stok et al. (2011); Foo, Lim and Wilson (2009); Chowienczyk, Kelly, Maccallum et al. (1999)]. Therefore, different physiological and pathological changes produce different waveform characteristics. However, for patients with type 2 diabetes, there is no research on the correlation between pulse waveform and arterial stiffness. Therefore, a comprehensive investigation into their pulse waveform characteristics is necessary. In this study, the pulse waveform data of patients with type 2 diabetes and healthy subjects were collected and characteristic parameters were extracted for statistical analysis. The correlation between baPWV used as the arterial stiffness index and pulse waveform parameters was analyzed to obtain the correlation between waveform parameters and arterial stiffness. The purpose of this study was to demonstrate that pulse waveform characteristics can be used as indices of arterial stiffness in patients with type 2 diabetes.

## 2. Method

### 2.1. Subjects

This study was based on the "Study on Evaluation Method of Cardiovascular System Based on Noninvasive Detection of Blood Pressure and Pulse Wave of Limbs" [Song, Li, Qiao et al. (2016)], which recruited over 400 subjects and determined their pulse wave and cardiovascular parameters. A total of 25 patients with type 2 diabetes and 50 healthy subjects registered at Beijing University of Technology Hospital in 2015 were included in this study. The measurements of baPWV and pulse waveform, and recording of basic information such as gender, height, and weight were also performed at the time. A total of 75 subjects fulfilled the

following criteria: exclusion of a diagnosis of limb disability, hypertension, arteriosclerosis, congenital heart disease, heart failure, and a history of artery intervention based on medical interviews, physical examinations, and screening examinations. Additionally, previous studies revealed a correlation between the arterial stiffness and the subjects' basic characteristics such as age and BMI [Mitchell, Parise, Benjamin et al. (2004)]. To avoid an influence of these factors on the results, there was no significant difference between the healthy subjects and the diabetics in this study in terms of age, height, weight, and other basic characteristics, which ensured that the change of pulse waveform was mainly caused by type 2 diabetes. The study protocol was approved by the Committee on the Ethics of Human Research of Beijing University of Technology. All participants provided written informed consents on the basis of a detailed understanding of the content of this study.

## 2.2. Pulse wave and baPWV measurement

Four limb pulse waves and blood pressure were measured using a Fukuda VS-1500A blood pressure and pulse measuring device (Fukuda Company, China) with the assistance of experienced doctors. All subjects were told the detection time several days in advance, and they were told not to eat stimulant food or drinks before the collection was completed. After resting for 15–20 min, each subject placed their hands on both sides of their body in a supine position. A phonocardiogram sensor was fixed in the second intercostal space on the sternum. Cuffs were fixed on the upper arms and ankles and electrodes were fixed at the left and right wrists. The device automatically obtained blood pressure and pulse waveform data of four limbs and automatically calculated the baPWV using the height of the subjects. The obtained data was stored in a database.
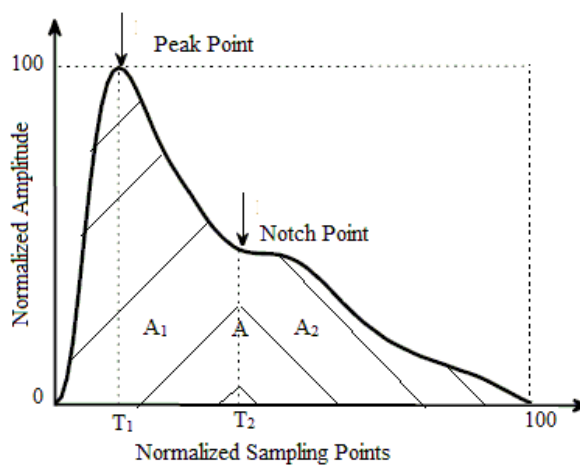
## 2.3. Pulse characteristics determination

### 2.3.1. Pulse waveforms denoising and normalization

First, the off-line signal processing was used on the pulse waves to remove the various noise signals introduced in the signal acquisition process [Chowienczyk, Kelly, Maccallum et al. (1999)]. Next, all the pulses of four limbs were averaged to obtain a single reference pulse (the averaged raw pulse) of every limb, as shown in Fig. 1a. According to the Nyquist theorem and the sampling frequency of the device, the averaged raw pulse was processed with a calibration for each period of 100 sampling points. This study focused on the pulse shape change. Thus, the pulse amplitude was calibrated to 0–100. An example of the processing result of one limb is shown in Fig. 1b. Following this, the pulse waveform characteristics were extracted.
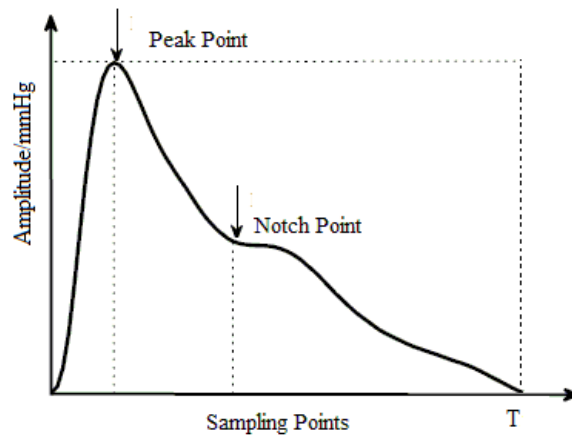
(a)



(b)

**Figure 1:** The pulse waveform characteristic extraction from the averaged raw pulse waveform (a) and

normalized pulse waveform (b)

*2.3.2. Pulse waveforms characteristics*

The pulse wave period (T), which was determined by the number of sampling points contained in the original waveform, was extracted from the averaged raw pulse as shown in Fig. 1a. The relative positions of the peak point ($T_1$) and notch point ($T_2$), total waveform area (A), and the areas of the waveform before ($A_1$) and after ($A_2$) the notch point were extracted from the calibrated pulse waveform as shown in Fig. 1b. These parameters can be used to characterize the arterial compliance of the subject as well as the artificial stiffness [Weber, Wassertheurer, Rammer et al. (2012); Li, Yang, Zhang et al.  (2007); Zhang, Wang, Zhang et al.  (2005); O'Rourke and MichaeIF (1982)].

During one cardiac cycle, the blood flow to the lower-extremity arteries takes longer than that in the upper limbs. Consequently, when using the starting point of the pulse wave period of the upper limb as a baseline, the pulse waveform of the lower-extremity arteries will be delayed. As shown in Fig. 2, the delay time

depends on the PWV in the lower-extremity arteries, which is directly influenced by the lower-extremity artery stiffness. Lower-extremity amputation and diabetic foot disease, which also have a direct relationship with the change of lower-extremity artery stiffness, are common complications of diabetes mellitus [Rith-Najarian and Reiber (2000)]. Therefore, the delay time ($T_3$), which is based on the number of original waveform acquisition points, was extracted as one of the characteristic parameters. The $T_3$ value can directly affect the calculated baPWV value. Compared with baPWV, measurement of $T_3$ is simpler and more accurate. This study analyzed the correlation between the $T_3$ parameters and the corresponding baPWV values to determine the typicality of the selected samples.
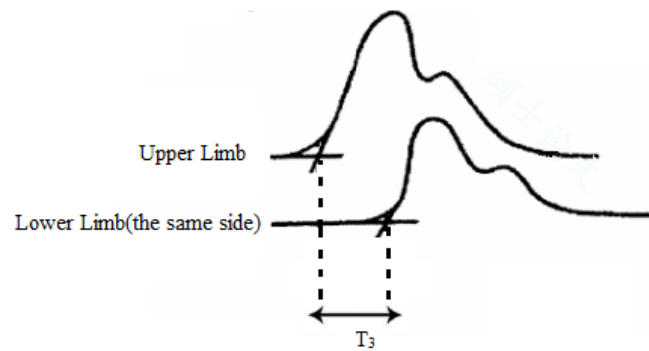


**Figure 2:** The determination of waveform characteristics $T_3$

### 2.4. Statistical analyses

The parameters were analyzed using the SPSS15.0 statistical software. The mean ± SD of the parameters (baPWV, blood pressure, and pulse pressure; and T, $T_1$, $T_2$, $T_3$, A, $A_1$, and $A_2$) was calculated for the healthy and diabetic subjects. An independent sample t-test was performed to determine whether there were significant differences in the parameters that we chose between healthy and diabetic subjects. Pearson's correlation analysis was used to determine the degree of correlation between pulse waveform parameters and baPWV, which was used as an index of arterial stiffness. A P value less than 0.05 was considered statistically significant.

## 3. Results

### 3.1. Result of independent samples T-test

Table 1 shows the basic characteristics of healthy and diabetic subjects. Compared with the healthy subjects group, the diabetic group differed significantly in terms of variables including the pulse pressure and systolic pressure (except at the left arm).

An independent sample t-test was also conducted on the two groups to determine the pulse waveform parameters that differed significantly between them. The results are presented in Table 2.

On comparing the pulse waveform parameters between these two groups, significant differences between

these parameters were observed, including in A, $A_1$, and $A_2$, which were separated by the dicrotic notch point, $T_3$ ($P < 0.05$). For the diabetic group, the values of A, $A_1$, and $A_2$ were higher than those of the healthy group, while the value of $T_3$ was lower than that of the healthy group. The remaining waveform parameters (pulse wave cycle T, the pulse peak position $T_1$, dicrotic notch position $T_2$) did not significantly differ between the two groups.

**Table 1:** Basic characteristics of the subjects with or without diabetes

| Characteristics | | Healthy | Diabetes | P |
|---|---|---|---|---|
| Number(male/female) | | 27/23 | 15/10 | —— |
| Age, (years) | | 63.3±3.4 | 65.9±4.1 | 0.2 |
| Height, (cm) | | 160.0±8.0 | 164.5±5.5 | 0.53 |
| Weight, (kg) | | 65.9±9.0 | 68.4±8.8 | 0.43 |
| Systolic Pressure, (mmHg) | Left Arm | 130.6±11.8 | 140.5±17.3 | 0.056 |
| | Right Arm | 129.3±9.5 | 139.0±16.0 | <0.05 |
| | Left Ankle | 144.1±19.2 | 161.8±18.6 | <0.05 |
| | Right Ankle | 145.0±18.8 | 162.1±19.1 | <0.05 |
| Diastolic Pressure, (mmHg) | Left Arm | 80.0±10.0 | 81.6±10.2 | 0.58 |
| | Right Arm | 80.1±7.6 | 80.0±10.3 | 0.92 |
| | Left Ankle | 74.9±7.4 | 76.0±8.2 | 0.68 |
| | Right Ankle | 77.3±7.4 | 79.8±10.4 | 0.41 |
| Pulse Pressure, (mmHg) | Left Arm | 50.9±8.6 | 58.9±10.8 | <0.05 |
| | Right Arm | 49.2±8.4 | 59.8±14.3 | <0.05 |
| | Left Ankle | 69.2±17.1 | 85.8±14.9 | <0.05 |
| | Right Ankle | 57.7±15.5 | 82.2±13.3 | <0.05 |

Data are presented as mean ± SD. P values were calculated using the independent samples T-test.

**Table 2:** The comparison of pulse waveform parameters between healthy and diabetes

| Characteristics | | Healthy | Diabetes | P |
|---|---|---|---|---|
| T | | 914.1±118.0 | 915.5±199.1 | 0.98 |
| $T_1$ | Left Arm | 22.8±4.1 | 23.4±4.0 | 0.67 |
| | Right Arm | 24.0±3.7 | 24.4±3.7 | 0.75 |
| | Left Ankle | 26.5±3.2 | 26.2±3.8 | 0.79 |
| | Right Ankle | 26.6±3.2 | 26.2±3.8 | 0.75 |
| $T_2$ | Left Arm | 38.6±3.3 | 38.8±5.5 | 0.92 |
| | Right Arm | 38.7±3.3 | 39.4±5.3 | 1262 |
| | Left Ankle | 52.7±5.0 | 52.9±7.5 | 0.92 |
| | Right Ankle | 52.8±5.1 | 53.2±7.6 | 0.83 |
| $T_3$ | | 83.2±14.2 | 72.4±10.4 | <0.05 |
| A | Left Arm | 6210.2±900.9 | 7506.2±858.5 | <0.05 |
| | Right Arm | 6098.8±1217 | 7453.1±1931.6 | <0.05 |
| | Left Ankle | 6717.9±1596.3 | 8375.2±1291.1 | <0.05 |
| | Right Ankle | 6566.0±1571.1 | 8180.5±1268.9 | <0.05 |
| $A_1$ | Left Arm | 3631.2±774.2 | 4343.0±961.1 | <0.05 |
| | Right Arm | 3524.0±945.1 | 4362.4±1395.6 | <0.05 |
| | Left Ankle | 5460.7±1404.5 | 6370.2±1160.1 | <0.05 |
| | Right Ankle | 5159.2±1298.7 | 6202.4±1323.7 | <0.05 |
| $A_2$ | Left Arm | 2421.9±279.9 | 2933.8±605.2 | <0.05 |
| | Right Arm | 2574.7±496.5 | 3090.8±911.7 | <0.05 |
| | Left Ankle | 1257.2±333.1 | 2005.0±601.9 | <0.05 |
| | Right Ankle | 1406.8±451.1 | 1978.1±562.2 | <0.05 |
| baPWV(m/s) | | 14.9±1.1 | 16.0±1.9 | <0.05 |

Data are presented as mean ± SD. P values were calculated using the independent samples T-test.

### 3.2. Pearson's correlation test

Previous studies demonstrated that baPWV is directly related to the incidence of type 2 diabetes, which can be used to assess the risk factors for diabetic complications. The baPWV can be used to characterize the arterial stiffness of patients with diabetes. The basic characteristics (pulse pressure and systolic pressure except for the left arm) and pulse waveform parameters (A, $A_1$, $A_2$, and $T_3$) were selected based on the results of the independent sample t-test, which showed that they differed significantly between these two groups. Next, Pearson's correlation test was performed between those parameters and the corresponding baPWV. The correlation between waveform parameters and the baPWV values was examined to investigate the correlation between the waveform parameters and the arterial stiffness. Pearson's correlation test results are presented in

Tables 3 and 4. The baseline characteristics of pulse pressure were significantly positively correlated with baPWV ($P < 0.05$). The systolic pressure except the left arm were significantly positively correlated with baPWV ($P < 0.05$).

**Table3:** Correlation between baseline characteristics and baPWV

| Characteristics | | R | P |
|---|---|---|---|
| Systolic Pressure, (mmHg) | Right Arm | 0.662** | <0.05 |
| | Left Ankle | 0.663** | <0.05 |
| | Right Ankle | 0.677** | <0.05 |
| | Left Arm | 0.512** | <0.05 |
| Pulse Pressure, (mmHg) | Right Arm | 0.474** | <0.05 |
| | Left Ankle | 0.556** | <0.05 |
| | Right Ankle | 0.549** | <0.05 |

P values were calculated using Pearson's correlation test.

*. Correlation is significant at the 0.05 level.

**. Correlation is significant at the 0.01 level.

**Table4:** Correlation between pulse waveform parameters and baPWV

| Characteristics | | R | P |
|---|---|---|---|
| A | Left Arm | 0.381* | <0.05 |
| | Right Arm | 0.369* | <0.05 |
| | Left Ankle | 0.458** | <0.05 |
| | Right Ankle | 0.434** | <0.05 |
| $A_1$ | Left Arm | 0.373* | <0.05 |
| | Right Arm | 0.342* | <0.05 |
| | Left Ankle | 0.410* | <0.05 |
| | Right Ankle | 0.396* | <0.05 |
| $A_2$ | Left Arm | 0.432** | <0.05 |
| | Right Arm | 0.275 | 0.110 |
| | Left Ankle | 0.340* | <0.05 |
| | Right Ankle | 0.269 | 0.118 |
| $T_3$ | | −0.458** | <0.05 |

P values were calculated using Pearson's correlation test.

*. Correlation is significant at the 0.05 level.

**. Correlation is significant at the 0.01 level.

The results showed that A and $A_1$ were significantly positively correlated with baPWV ($P < 0.05$). However, only $A_2$ of the left arm and left ankle was significantly positively correlated with baPWV ($P < 0.05$). The delay time $T_3$ was significantly negatively correlated with baPWV ($P < 0.05$).

## 4. Discussion and Conclusion

Pulse waveform analysis is an effective method to monitor and evaluate arterial vascular functions. Herein, the pulse waveform data from patients with type 2 diabetes and from healthy subjects were collected and characteristic parameters were extracted for statistical analysis. Next, the correlations between baPWV used as an index of arterial stiffness and pulse waveform parameters were analyzed to obtain the correlation between waveform parameters and arterial stiffness. Pulse area parameters (A, $A_1$, and $A_2$) showed significant differences ($P < 0.05$) between groups and had significant correlations ($P < 0.05$) with arterial stiffness. $T_3$ as a time parameter also provided the same statistical results. Thus, the pulse waveform parameters ($T_3$, A, $A_1$, and $A_2$) can be used as an index of arterial stiffness for patients with type 2 diabetes. This was the first study to comprehensively investigate the pulse wave shape and its characteristic differences between patients with type 2 diabetes and healthy subjects.

The waveform parameters selected in this study could have definitive physiological significance. The differences in pulse area parameters (A, $A_1$, and $A_2$) between patients with type 2 diabetes and healthy subjects was mainly determined by the difference in wave reflection timing. Previous studies reported that the wave reflection timing was primarily determined by arterial stiffness [Hirata, Kawakami and O'Rourke (2006); Mitchell, Parise, Benjamin et al. (2004)]. Therefore, it could be asserted that the differences in pulse area parameters between patients with type 2 diabetes and healthy subjects were caused by the changes in arterial stiffness. Pulse waves are the superposition of the pressure wave generated by the heart and the pressure wave reflected from the body in a cardiac cycle (Fig. 3). The reflected pressure wave can be divided into two types. Wave 1 was mainly reflected from the arterial branch during late systole or early diastole, whereas wave 2 was mainly caused by the collision between the blood and the closed aortic valve during diastole [Huang, Chang, Kao et al. (2010); Hirata, Kawakami and O'Rourke (2006); Mitchell, Parise, Benjamin et al. (2004)]. $A_1$ from the beginning to the notch point indicated the physiological characteristics of the cardiovascular system during systole. $A_1$ primarily depended on the pressure wave generated by the heart and the timing of wave 1. $A_2$ after the notch point depended on the timing of wave 1 and wave 2. In this study, increased pulse area parameters were observed for type 2 diabetic patients. The increase of A can be explained by the increase of $A_1$ and $A_2$, whereas the increase of $A_1$ and $A_2$ could be explained by the difference of wave reflection timing caused by a change in arterial stiffness. In healthy subjects, because of the low arterial stiffness resulting in a small baPWV value, wave 1 usually occurred near the notch point [Mitchell, Parise, Benjamin et al. (2004)]. Wave 1 had little influence on the amplitude and width of the main pulse wave, but influenced the dicrotic wave. In contrast, for patients with type 2 diabetes, the baPWV value was higher because of increased arterial stiffness. Wave 1 appeared early, and its relative position was close to the pressure wave generated by the heart, even with the superposition, which made $A_1$ higher due to the amplitude and width of the main pulse wave being increased. For patients with diabetes, although the high amplitude of wave 2 lead to high $A_2$, wave 1 made no contribution to the increase of $A_2$. Furthermore, previous studies reported that the changes in

peripheral resistance and blood viscosity also had a great influence on $A_2$ [Huang, Chang, Kao et al. (2010)]. This could be the reason for no significant correlation between baPWV and $A_2$ of the right arm and ankle. In this study, although $A_2$ could reflect the physiological characteristics during diastole, it had limitations as an index for characterizing the arterial stiffness.
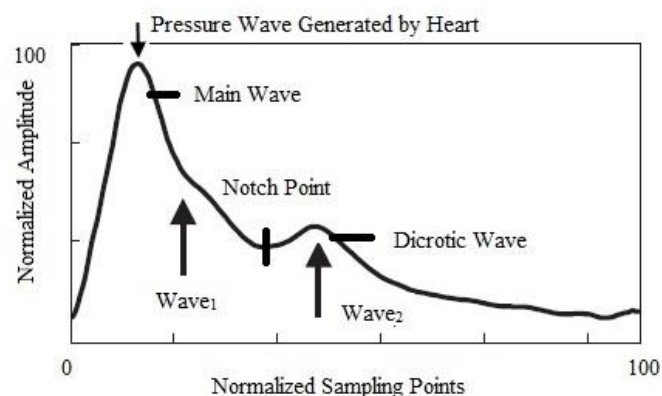


(a)
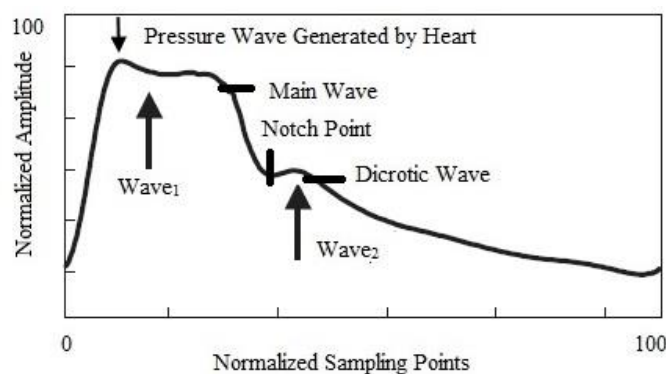


(b)

**Figure 3:** Determination of the pressure wave generated by the heart, reflection wave$_1$ and reflection wave$_2$. The arrow indicates the timing of the three waves. Compared with healthy people (a), the pulse area parameters of patients with type 2 diabetes patients (b) increased significantly.

We observed that pulse time parameters ($T$, $T_1$, and $T_2$) had no significant correlation ($P \gg 0.05$) with baPWV. This result was in agreement with those reported by previous studies describing that those time parameters were mainly determined by the condition of the heart function within one cardiac cycle, not the arterial stiffness change [Lacey and Lacey (1978)]. As for $T_3$, it was the time difference between the pulse wave of upper and lower limbs. $T_3$ showed statistically significant differences between groups and had a strong correlation with arterial stiffness. Previous studies reported that type 2 diabetic patients had a higher risk of peripheral arterial disease [Carmona, Hoffmeyer, Herrmann et al. (2005); Rith-Najarian and Reiber (2000)], which meant a significant increase in arterial stiffness of the lower limbs. This led to an increase in baPWV and reduction in $T_3$. Therefore, $T_3$ could reflect the change in arterial stiffness of the lower extremities in patients with type 2 diabetes. Combined with clinical data of lower-extremity vascular complications in type 2 diabetic patients, such as diabetic foot disease, a comprehensive analysis of $T_3$ and the development of

lower-extremity vascular complications should be carried out.

This study had several limitations, namely, the relatively limited number of patients with type 2 diabetes and the incomplete information on complications. A comprehensive comparison using additional clinical data on type 2 diabetes is warranted. The selected subjects have limitations in the basic physiological characteristics such as age, height and weight. The selected population cannot reflect the situation of patients with type 2 diabetes mellitus in all age groups and various somatotype. In this study, the statistical analysis results of blood pressure, pulse pressure, and baPWV from 75 subjects were consistent with those in previous studies. The results indicated that although the number of patients was not large, the participants' characteristics could represent the typical characteristics of the arterial vascular system in patients with type 2 diabetes. Expectedly, the pulse pressure and blood pressure of the diabetic group were higher than those of the healthy subjects. Elevated blood pressure and pulse pressure are more common in people with type 2 diabetes than in the general population [Schram, Kostense, Van Dijk et al. (2002); Adler, Stratton, Neil et al. (2000)]. The statistical analysis results of pulse pressure and blood pressure revealed that pulse pressure and systolic blood pressure could be used to determine the physiological status of arteries including arterial stiffness in patients with type 2 diabetes, while diastolic blood pressure had some limitations in this regard, which is in agreement with a previous study [Cockcroft, Wilkinson, Evans et al. (2005)]. The high baPWV value of patients with type 2 diabetes showed increased arterial stiffness compared with that in healthy subjects [Woolam, Schnur, Vallbona et al. (1962)], which is in line with the characteristics of arterial physiological and pathological changes in diabetic patients and was the theoretical basis of this study.

In conclusion, this study quantitatively demonstrated a significant change in the pulse waveform characteristics of patients with type 2 diabetes and analyzed the correlation between waveform parameters and arterial stiffness. This study showed that pulse waveform characteristics ($T_3$, $A$, $A_1$, and $A_2$) could be used as indices of arterial stiffness in patients with type 2 diabetes.

**References**

**Adler, A. I.; Stratton, I. M.; Neil, H. A.; Yudkin, J. S.; Matthews, D. R.; Cull, C. A. et al.** (2000): Association of systolic blood pressure with macrovascular and microvascular complications of type 2 diabetes (ukpds 36): prospective observational study. *British Medical Journal*, vol. 321, no. 7258, pp. 412-419.

**Allen, J.** (2007): Photoplethysmography and its application in clinical physiological measurement. *Physiological Measurement*, vol. 28, no. 3, pp. R1-R39.

**Aso, K.; Miyata, M.; Kubo, T.; Hashiguchi, H.; Fukudome, M.; Fukushige, E. et al.** (2003): Brachial-ankle pulse wave velocity is useful for evaluation of complications in type 2 diabetic patients. *Hypertension Research*, vol. 26, no. 10, pp. 807-813.

**Carmona, G. A.; Hoffmeyer, P.; Herrmann, F. R.; Vaucher, J.; Tschopp, O.; Lacraz, A. et al.** (2005): Major lower limb amputations in the elderly observed over ten years: the role of diabetes and peripheral arterial disease. *Diabetes & Metabolism*, vol. 31, no. 5, pp. 449-454.

**Chowienczyk, P. J.; Kelly, R. P.; Maccallum, H.; Millasseau, S. C.; Andersson, T. L.; Gosling, R. G. et al.** (1999): Photoplethysmographic assessment of pulse wave reflection: blunted response to endothelium-dependent beta2-adrenergic vasodilation in type ii diabetes mellitus. *Journal of the American College of Cardiology*, vol. 34, no. 7, pp. 2007-2014.

**Cockcroft, J. R.; Wilkinson, I. B.; Evans, M.; McEwan, P.; Peters, J. R.; Davies, S. et al.** (2005): Pulse pressure predicts cardiovascular risk in patients with type 2 diabetes mellitus. *American Journal of Hypertension*, vol. 18, no. 11, pp. 1463-1467.

**Foo, J. Y.; Lim, C. S.; Wilson, S. J.** (2009): Photoplethysmographic assessment of hemodynamic variations using pulsatile tissue blood volume. *Angiology*, vol. 59, no. 6, pp. 745-752.

**Hasegawa, S.; Sato, S.; Numano, F.; Park, J.; Hoshina, S.; Endoh, H. et al.** (2011): Characteristic alteration in the second derivative of photoplethysmogram in children. *Pediatrics International*, vol. 53, no. 2, pp. 154-158.

**Hirata, K.; Kawakami, M.; O'Rourke, M. F.** (2006): Pulse wave analysis and pulse wave velocity: a review of blood pressure interpretation 100 years after korotkov. *Circulation Journal Official Journal of the Japanese Circulation Society*, vol. 70, no. 10, pp. 1231-1239.

**Huang, C. M.; Chang, H. C.; Shung-Te, K.; Li, T. C.; Wei, C. C.; Chen, C. et al.** (2010): Radial pressure pulse and heart rate variability in heat- and cold-stressed humans. *Evidence-Based Complementary and Alternative Medicine*, vol. 2011, no. 751317, pp. 1-9.

**Hughes, S. M.; Dixon, L. J.; Mcveigh, G. E.** (2004): Arterial stiffness and pulse wave velocity: problems with terminology. *Circulation*, vol. 109, no. 2, pp. e3.

**Ibata, J.; Sasaki, H.; Kakimoto, T.; Matsuno, S.; Nakatani, M.; Kobayashi, M. et al.** (2008): Cardio-ankle vascular index measures arterial wall stiffness independent of blood pressure. *Diabetes Research*

*and Clinical Practice*, vol. 80, no. 2, pp. 265-270.

**Lacey, B. C.; Lacey, J. I.** (1978): Two-way communication between the heart and the brain. significance of time within the cardiac cycle. *American Psychologist*, vol. 33, no. 2, pp. 99-113.

**Li, J.; Yang, L.; Zhang, S.; Yang, Y.** (2007): Computation of cardiac output by pulse wave contour. *International Conference on Bioinformatics and Biomedical Engineering*, pp. 1088-1090.

**Maeda, Y.; Inoguchi, T.; Etoh, E.; Kodama, Y.; Sasaki, S.; Sonoda, N. et al.** (2014): Brachial-ankle pulse wave velocity predicts all-cause mortality and cardiovascular events in patients with diabetes: the kyushu prevention study of atherosclerosis. *Diabetes Care*, vol. 37, no. 8, pp. 2383-2390.

**Mitchell, G. F.; Parise, H.; Benjamin, E. J.; Larson, M. G.; Keyes, M. J.; Vita, J. A. et al.** (2004): Changes in arterial stiffness and wave reflection with advancing age in healthy men and women: the framingham heart study. *Hypertension*, vol. 43, no. 6, pp. 1239-1245.

**O'Rourke; MichaeIF.** (1982): *Arterial function in health and disease.* Churchill livingstone, USA.

**Rith-Najarian, S. J.; Reiber, G. E.** (2000): Prevention of Foot Problems in Persons with Diabetes. *Journal of Family Practice*, vol. 49, no. Suppl11, pp. S30.

**Rydén, L.; Standl, E.; Małgorzata, B.; Van Den Berghe, G.; Betteridge, J.; De Boer, M. J. et al.** (2007): Guidelines on diabetes, pre-diabetes, and cardiovascular diseases: executive summary. *European Heart Journal*, vol. 28, no. 1, pp. 88-136.

**Schram, M. T.; Kostense, P. J.; Van Dijk, R. A.; Dekker, J. M.; Nijpels, G.; Bouter, L. M. et al.** (2002): Diabetes, pulse pressure and cardiovascular mortality: the hoorn study. *Journal of Hypertension*, vol. 20, no. 9, pp. 1743-1751.

**Shirai, K.; Hiruta, N.; Song, M.; Kurosu, T.; Suzuki, J.; Tomaru, T. et al.** (2011): Cardio-ankle vascular index (cavi) as a novel indicator of arterial stiffness: theory, evidence and perspectives. *Journal of Atherosclerosis & Thrombosis*, vol. 18, no. 11, pp. 924-938.

**Song, X. R.; Li, G. Y.; Qiao, A. K.; Chen, Z. H.** (2016): Association of simultaneously measured four-limb blood pressures with cardiovascular function: a cross-sectional study. *BioMedical Engineering OnLine,* vol. 15, no. Suppl2, pp. 247-260.

**Weber, T.; Wassertheurer, S.; Rammer, M.; Haiden, A.; Hametner, B.; Eber, B.** (2012): Wave reflections, assessed with a novel method for pulse wave separation, are associated with end-organ damage and clinical outcomes. *Hypertension*, vol. 60, no. 2, pp. 534-541.

**Westerhof, B. E.; Guelen, I.; Stok, W. J.; Wesseling, K. H.; Spaan, J. A.; Westerhof, N. et al.** (2007): Arterial pressure transfer characteristics: effects of travel time. *American Journal of Physiology-Heart and Circulatory Physiology*, vol. 292, no. 2, pp. H800-H807.

**Woolam, G. L.; Schnur, P. L.; Vallbona, C.; Hoff, HE.** (1962): The pulse wave velocity as an early indicator of atherosclerosis in diabetic subjects. *Circulation*, vol. 25, no. 3, pp. 533-539.

**Zhang, K. X.; Wang, Y.; Zhang, S.; Yang, Y. M.; Luo, Z, C.; Zeng, Y. J.** (2005): Dynamic analysis for blood flow parameters of cardiovascular system on work load. *Engineering in Medicine and Biology Society, 2005. Ieee-Embs 2005. International Conference of the IEEE,* Vol. 5, pp. 5551-5554.